

<sup>1</sup>  
<sup>2</sup> Susceptible host dynamics explain pathogen resilience to  
<sup>3</sup> perturbations

<sup>4</sup>

<sup>5</sup> Sang Woo Park, . . . , Bryan T. Grenfell, Sarah Cobey

## <sup>6</sup> Abstract

<sup>7</sup> A major priority for epidemiological research in the time of anthropogenic change  
<sup>8</sup> is understanding how infectious disease dynamics respond to perturbations. Inter-  
<sup>9</sup> ventions to slow the spread of SARS-CoV-2 significantly disrupted the transmission  
<sup>10</sup> of other human pathogens. As interventions lifted, whether and when respiratory  
<sup>11</sup> pathogens would eventually return to their pre-pandemic dynamics remains to be  
<sup>12</sup> answered. Here, we present a framework for estimating pathogen resilience based on  
<sup>13</sup> how fast epidemic patterns return to their pre-pandemic, endemic dynamics and an-  
<sup>14</sup> alyze time series data from Hong Kong, Canada, Korea, and the US. By quantifying  
<sup>15</sup> the resilience of common respiratory pathogens, we are able to predict when each  
<sup>16</sup> pathogen will eventually return to its pre-pandemic, endemic dynamics. Our pre-  
<sup>17</sup> dictions closely match the observed deviations (or lack thereof) from its pre-COVID  
<sup>18</sup> dynamics. Discrepancies between predicted and observed dynamics indicate the  
<sup>19</sup> long-term impact of pandemic perturbations, suggesting that some pathogens may  
<sup>20</sup> be converging to a different endemic cycle. Finally, we show that the replenishment  
<sup>21</sup> rate of the susceptible pool is a key determinant of pathogen resilience, which in  
<sup>22</sup> turn determines the sensitivity of a system to stochastic perturbations. Overall, our  
<sup>23</sup> analysis highlights the persistent nature of common respiratory pathogens compared  
<sup>24</sup> to vaccine-preventable infections, such as measles.

25 Non-pharmaceutical interventions to slow the spread of SARS-CoV-2 disrupted  
 26 the transmission of other human respiratory pathogens, adding uncertainties to their  
 27 future epidemic dynamics and their public health burden [1]. As interventions lifted,  
 28 large heterogeneities in outbreak dynamics were observed across different pathogens  
 29 in different countries, with some pathogens exhibiting earlier and faster resurgences  
 30 than others [2, 3, 4]. Heterogeneities in the overall reduction in transmission and the  
 31 timing of re-emergence likely reflect differences in intervention patterns, pathogen  
 32 characteristics, immigration/importation from other countries, and pre-pandemic  
 33 pathogen dynamics [5]. Therefore, comparing the differential impact of the pan-  
 34 *demic* perturbations across pathogens can provide unique opportunities to learn  
 35 about underlying pathogen characteristics, such as their transmissibility or duration  
 36 of immunity, from heterogeneities in re-emergence patterns [6].

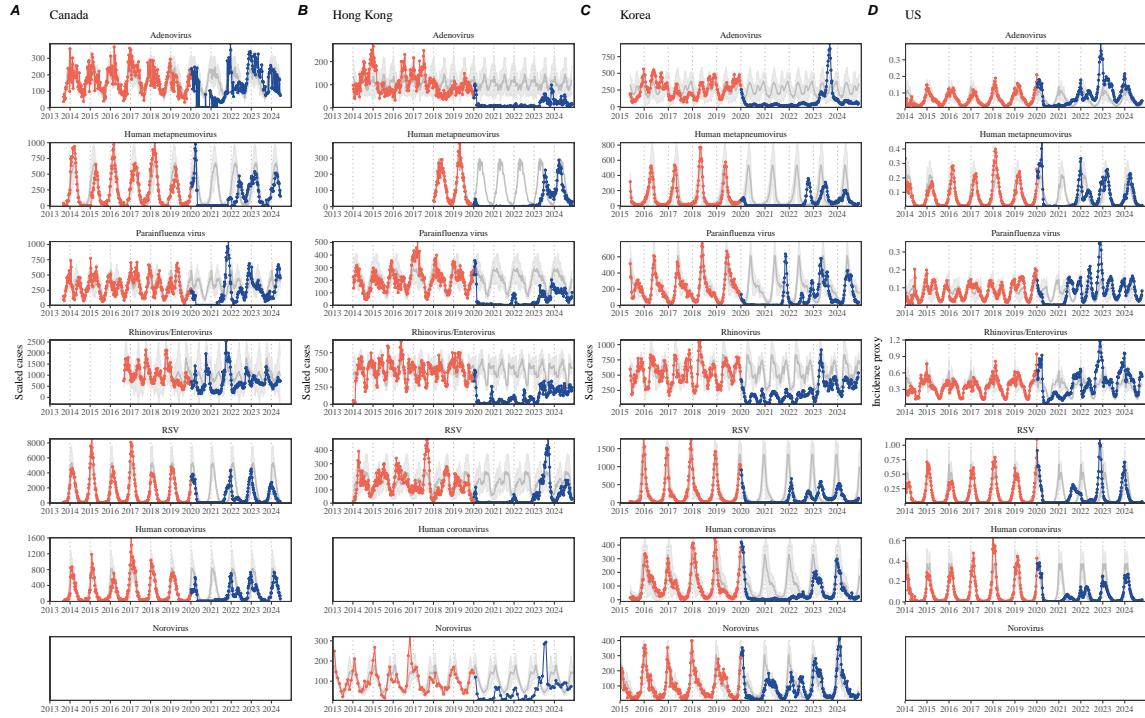


**Figure 1: Observed heterogeneity in responses to pandemic perturbations across respiratory pathogens and norovirus in (A) Canada, (B) Hong Kong, (C) Korea, and (D) US.** Red points and lines represent data before 2020. Blue points and lines represent data since 2020. Gray lines and shaded regions represent the mean seasonal patterns and corresponding 95% confidence intervals around the mean. Mean seasonal patterns were calculated by aggregating cases before 2020 into 52 weekly bins and taking the average in each week. Cases were scaled to account for changes in testing patterns (Materials and Methods).

37 Even though more than five years have passed since the emergence of SARS-CoV-  
 38 2, we still observe persistent changes in pathogen dynamics following the pandemic

39 perturbations. For example, compared to pre-pandemic, seasonal patterns, human  
40 metapneumovirus in Korea seem to circulate at lower levels, whereas RSV in Korea  
41 seems to exhibit different seasonality (Figure 1). These observations suggest a funda-  
42 mental change in pathogen dynamics following the pandemic perturbations, which  
43 might be driven by a long-term shift in either human behavior or population-level  
44 immunity [7, 8]. For example, the emergence of SARS-CoV-2 could have caused  
45 a long-term shift in population-level immunity through its interactions with other  
46 pathogens [9], especially with seasonal coronaviruses [7, 10, 11]. The possibility of a  
47 long-lasting impact of the pandemic perturbations poses an important question for  
48 future infectious disease dynamics: can we predict whether and when other pathogens  
49 will eventually return to their pre-pandemic dynamics?

50 So far, most analyses of respiratory pathogens after pandemic perturbations have  
51 focused on characterizing the timing of rebound [1, 12, 5]. Instead, we seek to char-  
52 acterize how fast (and whether) a pathogen returns to its pre-pandemic dynamics.  
53 These two concepts have a subtle but important difference. For example, it took  
54 more than 3 years for human metapneumovirus to rebound in Hong Kong, but the  
55 observed epidemic patterns in 2024 are similar to pre-pandemic seasonal means, sug-  
56 gesting a rapid return to pre-pandemic dynamics (Figure 1). Measuring this rate of  
57 return is useful because it allows us to quantify the ecological resilience of a host-  
58 pathogen system, which can inform responses to future interventions [13, 14, 15, 16].

59 In this study, we lay out theoretical and statistical approaches to characterizing  
60 the resilience of a host-pathogen system based on how fast the system recovers from  
61 perturbation. We begin by laying out a few representative scenarios that capture the  
62 potential impact of pandemic perturbations on endemic pathogen dynamics and illus-  
63 trate how resilience can be measured by comparing the pre- and post-pandemic dy-  
64 namics of susceptible and infected hosts. In practice, information on susceptible hosts  
65 is often unavailable, making this theoretical approach infeasible. Instead, we utilize a  
66 mathematical technique to reconstruct empirical attractors from the data [17], which  
67 allows us to measure the rate at which the host-pathogen system approaches this em-  
68 pirical attractor after a perturbation; this rate corresponds to the resilience of the  
69 host-pathogen system. We use this method to analyze pathogen surveillance data for  
70 respiratory and non-respiratory pathogens from Canada, Hong Kong, Korea, and the  
71 US. Finally, we show that susceptible host dynamics explain variation in pathogen  
72 resilience and further demonstrate that more resilient pathogens will be less sensitive  
73 to perturbations caused by demographic stochasticity, thereby providing a direct link  
74 between pathogen resilience and persistence.

## 75 **Conceptual introduction to pathogen resilience**

76 In classical ecological literature, the resilience of an ecological system is measured by  
77 the rate at which the system returns to its reference state following a perturbation  
78 [13, 14, 15, 16]. This rate corresponds to the largest real part of the eigenvalues of

79 the linearized system near equilibrium—here, we refer to this value as the *intrinsic*  
80 resilience of the system, which represents the expected rate of return from perturbed  
81 states. In practice, we rarely know the true model describing population-level dy-  
82 namics of common respiratory pathogens, limiting our ability to infer the intrinsic  
83 resilience of a system. Instead, we can still measure the *empirical* resilience of a  
84 host-pathogen system by looking at how fast the system returns to the pre-pandemic,  
85 endemic dynamics after pandemic perturbations are lifted.

86 As an example, we begin with a simple Susceptible-Infected-Recovered-Susceptible  
87 (SIRS) model with seasonally forced transmission and demography (i.e., birth and  
88 death). The SIRS model is the simplest model that allows for the waning of im-  
89 munity and is commonly used for modeling the dynamics of respiratory pathogens  
90 [18]. First, consider a pandemic perturbation that reduces transmission by 50% for 6  
91 months starting in 2020, which causes epidemic patterns to deviate from their origi-  
92 nal stable annual cycle for a short period of time and eventually come back (Figure  
93 2A). To measure the resilience of this system empirically, we first need to be able to  
94 measure the distance from its pre-pandemic attractor. There are many ways we can  
95 measure the distance from the attractor, but for illustrative purposes, we choose one  
96 of the most parsimonious approaches: that is, we look at how the susceptible (S) and  
97 infected (I) populations change over time and measure the distance on the SI phase  
98 plane (Figure 2B). In this simple case, the locally estimated scatterplot smoothing  
99 (LOESS) fit indicates that the distance from the attractor decreases exponentially  
100 (linearly on a log scale) on average (Figure 2C). Furthermore, the overall rate of re-  
101 turn approximates the intrinsic resilience of the seasonally unforced system (Figure  
102 2C).

103 Alternatively, pandemic perturbations can have a lasting impact on the pathogen  
104 dynamics; as an example, we consider a scenario in which a 10% reduction in trans-  
105 mission persists even after the major pandemic perturbations are lifted (Figure 2D–  
106 F). In such cases, we cannot know whether the pathogen will return to its original  
107 cycle or a different cycle until many years have passed, and we cannot measure the  
108 distance to the new unknown attractor that the system might eventually approach.  
109 Nonetheless, we can still measure the distance from the pre-pandemic attractor and  
110 ask how the distance changes over time (Figure 2E). The LOESS fit suggests that the  
111 distance from the pre-pandemic attractor will initially decrease exponentially on av-  
112 erage (equivalently, linearly on a log scale) and eventually plateau (Figure 2F). Here,  
113 a permanent 10% reduction in transmission rate slows the system, which causes the  
114 distance from the pre-pandemic attractor initially to decrease at a slower rate (Figure  
115 2F) than it would have otherwise (Figure 2C) before plateauing at a fixed distance  
116 between the two attractors. This example shows that resilience is not necessarily an  
117 intrinsic property of a specific pathogen. Instead, pathogen resilience is a property  
118 of a specific attractor that a host-pathogen system approaches, which depends on  
119 both pathogen and host characteristics.

120 Finally, transient phenomena can further complicate the picture (Figure 2G–I).  
121 For example, a stage-structured model initially exhibits a stable annual cycle, but

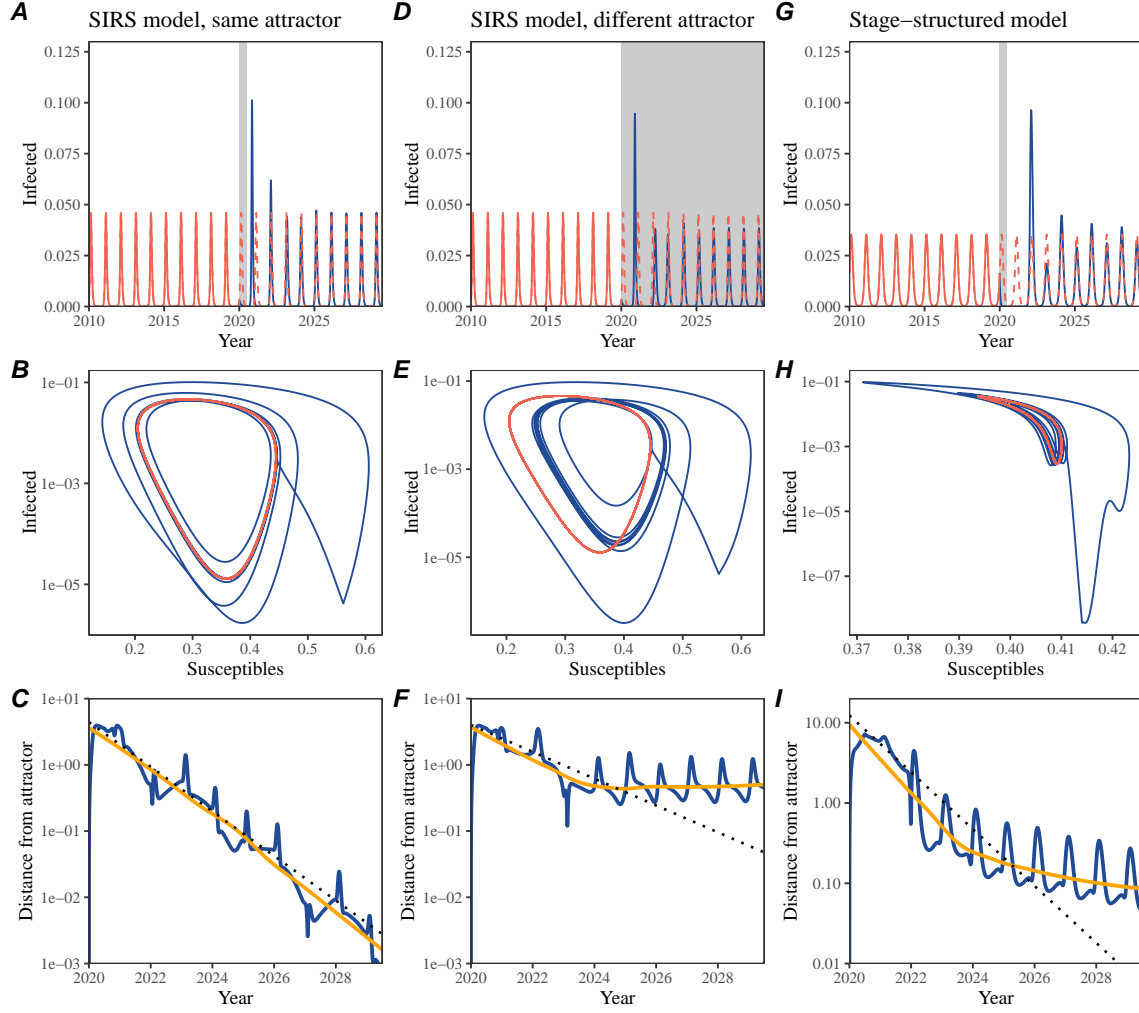


**Figure 2: A simple method to measure pathogen resilience following pandemic perturbations across different scenarios.** (A, D, G) Simulated epidemic trajectories across various models. Red and blue solid lines represent epidemic dynamics before and after pandemic perturbations are introduced, respectively. Red dashed lines represent counterfactual epidemic dynamics in the absence of perturbations. Gray regions indicate the duration of perturbations. (B, E, H) Phase plane representation of the time series in panels A, D, and G alongside the corresponding susceptible host dynamics. Red and blue solid lines represent epidemic trajectories on an SI phase plane before and after perturbations are introduced, respectively. (C, F, I) Changes in logged distance from the attractor over time. Blue lines represent the logged distance from the attractor. Orange lines represent the locally estimated scatterplot smoothing (LOESS) fits to the logged distance from the attractor. Dotted lines show the intrinsic resilience of the seasonally unforced system.

122 perturbations from a 10% reduction in transmission for 6 months cause the epidemic

123 to shift to biennial cycles (Figure 2G). The system eventually approaches the original  
124 pre-pandemic attractor (Figure 2H), suggesting that this biennial cycle is a transient  
125 phenomenon. The LOESS fit indicates that the distance from the attractor initially  
126 decreases exponentially at a rate that is consistent with the intrinsic resilience of  
127 the seasonally unforced stage-structured system, but the rate of decrease decelerates  
128 with the damped oscillations (Figure 2I). This behavior is also referred to as a ghost  
129 attractor, which causes long transient dynamics and slow transitions [19]. Strong  
130 seasonal forcing in transmission can also lead to transient phenomena for a simple  
131 SIRS model, causing a slow return to pre-perturbation dynamics (Supplementary  
132 Figure S1).

133 This empirical approach allows us to measure the resilience of a two-strain host-  
134 pathogen system even when we have incomplete observation of the infection dynam-  
135 ics. Simulations from a simple two-strain competition system illustrate that separate  
136 analyses of individual strain dynamics (e.g., RSV A vs B) and a joint analysis of total  
137 infections (e.g., total RSV infections) yield identical resilience estimates (Supplemen-  
138 tary Figure S2, 3). This is expected because the dynamics of two strains (or two  
139 pathogens) around the attractor in a coupled system are described by the same set  
140 of eigenvalues and eigenvectors, meaning that both strains should exhibit identical  
141 rates of returns following a perturbation. Analogous to a single system, strong sea-  
142 sonal forcing in transmission can cause the system to slow down through transient  
143 phenomena (Supplementary Figure S4).

144 These observations yield three insights. First, we can directly estimate the empirical  
145 resilience of a host-pathogen system by measuring the rate at which the system  
146 approaches an attractor, provided that we have a way to quantify the distance from  
147 the attractor. The empirical approach to estimating pathogen resilience is particu-  
148 larly convenient because it does not require us to know the true underlying model;  
149 estimating the intrinsic resilience from fitting misspecified models can lead to biased  
150 estimates (Supplementary Figure S5). Second, resilience estimates allow us to make  
151 phenomenological predictions about the dynamics of a host-pathogen system follow-  
152 ing a perturbation. Assuming that an attractor has not changed and the distance  
153 from the attractor will decrease exponentially over time, we can obtain a ballpark  
154 estimate for when the system should reach an attractor. Finally, a change in the rate  
155 of an exponential decrease in the distance from the attractor can provide information  
156 about whether the system has reached an alternative attractor, or a ghost attractor,  
157 that is different from the original, pre-pandemic attractor. These alternative attrac-  
158 tors may reflect continued perturbations from permanent changes in transmission  
159 patterns as well as changes in immune landscapes. There will be periods of time  
160 when it is difficult to tell whether pathogen dynamics are still diverging from the  
161 original attractor or have begun to converge to a new attractor; now that several  
162 years have passed since interventions have been lifted, we expect many respiratory  
163 pathogens to have had sufficient time to begin returning to their post-intervention  
164 attractors. With recent data, we can start to evaluate whether we see early signs of  
165 convergence to the former attractor or a new one.

166 **Inferring pathogen resilience from real data**

167 Based on these observations, we now lay out our approach to estimating pathogen  
168 resilience from real data (Figure 3). We first tested this approach against simulations  
169 and applied it to real data. Specifically, we analyzed case time series of respiratory  
170 pathogens from four countries: Canada, Hong Kong, Korea, and the US.

171 So far, we have focused on simple examples that assume a constant transmission  
172 reduction during the pandemic. However, in practice, the impact of pandemic per-  
173 turbations on pathogen transmission was likely more complex (Figure 3A), reflecting  
174 introduction and relaxation of various intervention strategies. In some cases, strong  
175 perturbations likely caused local fadeouts, requiring immigration from another loca-  
176 tion for epidemic rebound. Such complexities could lead to longer delays between  
177 the introduction of pandemic perturbations and pathogen rebound as well as tempo-  
178 ral variation in outbreak sizes (Figure 3B): in this example, continued transmission  
179 reduction from interventions limits the size of the first outbreak in 2021 following  
180 the rebound, allowing for a larger outbreak in 2022 when interventions are further  
181 relaxed.

182 Previously, we relied on the dynamics of susceptible and infected hosts to com-  
183 pute the distance from the attractor (Figure 2), but information on susceptible hosts  
184 is rarely available in practice. In addition, uncertainties in case counts due to ob-  
185 servation error, strain evolution, and multiannual cycles in the observed epidemic  
186 dynamics (e.g., adenovirus circulation patterns in Hong Kong and Korea) add chal-  
187 lenges to defining pre-pandemic attractors, which limits our ability to measure the  
188 distance from the attractor. To address these challenges, we can reconstruct an em-  
189 pirical attractor by utilizing Takens' theorem [17], which states that an attractor of a  
190 nonlinear multidimensional system can be mapped onto a delayed embedding (Mate-  
191 rials and Methods). For example, we can use delayed logged values of pre-pandemic  
192 cases  $C(t)$  (Figure 3C) to reconstruct the attractor:

$$\langle \log(C(t) + 1), \log(C(t - \tau) + 1), \dots, \log(C(t - (M - 1)\tau) + 1) \rangle, \quad (1)$$

193 where the delay  $\tau$  and embedding dimension  $M$  are determined based on autocor-  
194 relations and false nearest neighbors, respectively [20, 21]. We can then apply the  
195 same delay and embedding dimensions to the entire time series to determine the po-  
196 sition in multi-dimensional state space (Figure 3D), which allows us to measure the  
197 nearest neighbor distance between the current state of the system and the empirical  
198 pre-pandemic attractor (Figure 3E). In theory, we can now quantify how fast this  
199 distance decreases by fitting a linear regression on a log scale, where the slope of  
200 the linear regression empirically measures pathogen resilience. However, resulting  
201 estimates of pathogen resilience can be sensitive to choices about embedding delays  
202 and dimensions. For example, using longer delays and higher dimensions tends to  
203 smooth out temporal variations in the distance from the attractor (Supplementary  
204 Figure S6).

205 Complex changes in the distance from the attractor suggest that estimating

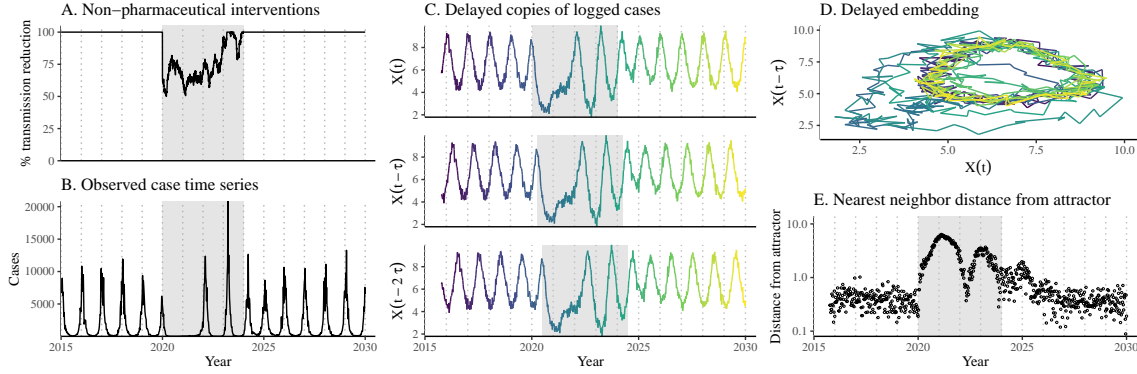


Figure 3: **A schematic diagram explaining the inference of pathogen resilience from synthetic data.** (A) A realistic example of simulated pandemic perturbations, represented by a relative reduction in transmission. (B) The impact of the synthetic pandemic perturbation on epidemic dynamics simulated using a SIRS model with demographic stochasticity. (C) Generating delayed copies of the logged time series allows us to obtain an embedding. (D) Two dimensional representation of an embedding. (E) Delayed embedding allows us to calculate the nearest neighbor distance from the empirical attractor, which is determined based on the pre-pandemic time series. This distance time series can be used to infer pathogen resilience after choosing an appropriate window for linear regression.

206 pathogen resilience from linear regression will be particularly sensitive to our choice  
 207 of fitting windows for the regression (Figure 3E). Therefore, before we tried estimat-  
 208 ing resilience from real data, we explored an automated window selection criterion  
 209 for linear regression and tested it against randomized, stochastic simulations across  
 210 a range of realistic pandemic perturbation shapes. In doing so, we also explored  
 211 optimal choices for embedding dimensions and evaluated our choices of fitting win-  
 212 dow parameters and embedding dimensions by quantifying correlation coefficients  
 213 between the estimated resilience and the intrinsic resilience of a seasonally unforced  
 214 system (Materials and Methods). Overall, we found large variation in estimation  
 215 performances with correlation coefficient ranging from 0.21 to 0.61 (Supplementary  
 216 Figure S7). In almost all cases, the automated window selection approach outper-  
 217 formed a naive approach that uses the time series, starting from the peak distance  
 218 (Supplementary Figure S7).

219 Based on the best performing window selection criteria and embedding dimen-  
 220 sion, we applied this approach to pathogen surveillance data presented in Figure  
 221 1 (Materials and Methods). For each time series, we applied Takens' theorem in-  
 222 dependently to reconstruct the empirical attractor and obtained the corresponding  
 223 time series of distances from attractors (Supplementary Figure S8). Then, we used  
 224 the automated window selection criterion to fit a linear regression and estimated the  
 225 empirical resilience for each pathogen in each country (Supplementary Figure S8);  
 226 the window selection criterion gave poor regression window for three cases (norovirus

227 in Hong Kong and Korea and rhinovirus/enterovirus in the US), leading to unrealistically low resilience estimates, and so we used ad-hoc regression windows instead  
228 (Supplementary Figure S9; Materials and Methods).

230 For all pathogens we considered, resilience estimates fell between 0.4/year and  
231 1.8/year (Figure 4A). We estimated the mean resilience of common respiratory  
232 pathogens to be 0.99/year (95% CI: 0.81/year–1.18/year). For reference, this is  
233  $\approx$  7.5 times higher than the intrinsic resilience of pre-vaccination measles in England  
234 and Wales ( $\approx$  0.13/year). Finally, resilience estimates for norovirus were comparable  
235 to those of common respiratory pathogens: 1.44/year (95%CI: 1.01/year–1.87/year)  
236 for Hong Kong and 1.07/year (95%CI: 0.86/year–1.29/year) for Korea. Based on  
237 a simple ANOVA test, we did not find significant differences in resilience estimates  
238 across countries ( $p = 0.25$ ) or pathogens ( $p = 0.67$ ).

239 Using resilience estimates, we predicted when each pathogen would hypothetically  
240 return to their pre-pandemic dynamics, assuming no long-term change in the attractor.  
241 Specifically, we extended our linear regression fits to distance-from-attractor  
242 time series and ask when the predicted regression line will cross a threshold value;  
243 since we relied on nearest neighbor distances, pre-pandemic distances are always  
244 greater than zero (Figure 3E), meaning that we can use the mean of pre-pandemic  
245 distances as our threshold.

246 We predicted that a return to pre-pandemic cycles has occurred would be im-  
247 minent for most pathogens (Figure 4B). In particular, we predicted that 12 out of  
248 23 pathogen-country pairs should have already returned before the end of 2024. For  
249 almost all pathogens that were predicted to have returned already, the observed  
250 epidemic dynamics showed clear convergence towards their pre-pandemic seasonal  
251 averages, confirming our predictions (Figure 4C). However, there were a few ex-  
252 ceptions, including norovirus in Hong Kong and rhinovirus/enterovirus in the US,  
253 where the observed epidemic dynamics in 2024 exhibit clear deviation from their pre-  
254 pandemic seasonal averages (Figure 4C; Figure S9). These observations suggest a  
255 possibility that some common respiratory pathogens may have converged to different  
256 attractors or are still exhibiting non-equilibrium dynamics. In contrast, pathogens  
257 that were predicted to have not returned yet also showed clear differences from their  
258 pre-pandemic seasonal averages; as many of these pathogens are predicted to return  
259 in 2025–2026, we may be able to test these predictions in near future (Supplementary  
260 Figure S10). Our reconstructions of distance time series and estimates of pathogen  
261 resilience and expected return time were generally robust to choices of embedding  
262 dimensions (Supplementary Figure S11–12).

## 263 **Susceptible host dynamics explain variation in pathogen 264 resilience**

265 So far, we have focused on quantifying pathogen resilience from the observed pat-  
266 terns of pathogen re-emergence following pandemic perturbations. But what factors

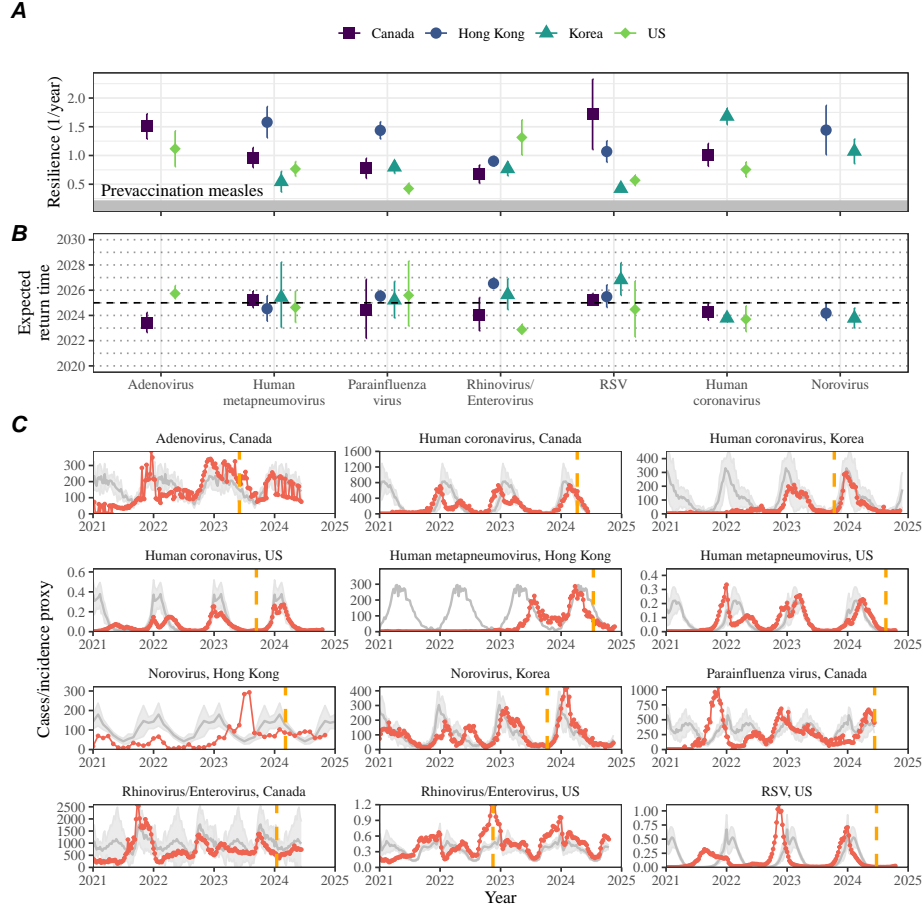
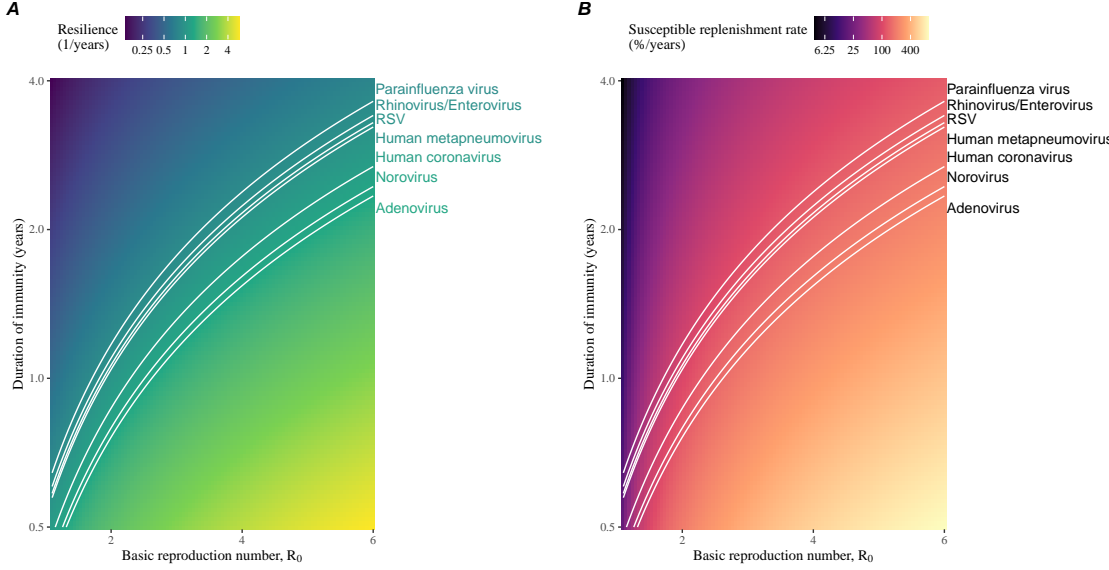


Figure 4: **Summary of resilience estimates and predictions for return time.** (A) Estimated pathogen resilience. The gray horizontal line represents the intrinsic resilience of pre-vaccination measles dynamics. (B) Predicted timing of when each pathogen will return to their pre-pandemic cycles. The dashed line in panel B indicates the end of 2024. Error bars represent 95% confidence intervals. (C) Observed dynamics for pathogen that are predicted to have returned before the end of 2024. Red points and lines represent data before 2020. Gray lines and shaded regions represent the mean seasonal patterns and corresponding 95% confidence intervals around the mean, previously shown in Figure 1. Orange vertical lines represent the predicted timing of return.

determine how resilient a host-pathogen system is? To address this question, we used the SIRS model to explore how changes in susceptible host dynamics affect pathogen resilience. To do so, we varied the basic reproduction number  $\mathcal{R}_0$ , which represents the average number of secondary infections caused by a newly infected individual in a fully susceptible population, and the duration of immunity and computed intrinsic resilience for each parameter.



**Figure 5: Linking pathogen resilience to epidemiological parameters and susceptible host dynamics.** (A) Intrinsic resilience as a function of the basic reproduction number  $\mathcal{R}_0$  and the duration of immunity. (B) Per-capita susceptible replenishment rate as a function of the basic reproduction number  $\mathcal{R}_0$  and the duration of immunity. The standard SIRS model without seasonal forcing is used to compute intrinsic resilience and the per-capita susceptible replenishment rate. Lines correspond to a set of parameters that are consistent with mean resilience estimates for each pathogen, averaged across different countries.

We found that an increase in  $\mathcal{R}_0$  and a decrease in the duration of immunity correspond to an increase in pathogen resilience (Figure 5A). Similarly, an increase in  $\mathcal{R}_0$  and a decrease in the duration of immunity corresponds to a faster per-capita rate of susceptible replenishment, which is defined as the ratio between absolute rate at which new susceptibles enter the population and the equilibrium number of susceptible individuals in the population,  $S^*$  (Figure 5B). We note that a higher  $\mathcal{R}_0$  drives a faster per-capita susceptible replenishment rate by decreasing the susceptible proportion at equilibrium,  $S^*$ . For a simple SIR model that assumes a life-long immunity, we can show analytically that pathogen resilience is proportional to the per-capita rate of susceptible replenishment (Materials and Methods). Overall, these observations suggest that a faster per-capita susceptible replenishment rate causes the system to be more resilient.

By taking the average values of empirical resilience values for each pathogen, we were able to map each pathogen onto a set of parameters of the SIRS model that are consistent with corresponding resilience estimates (Figure 5A). Across all pathogens we considered, we estimated that the average duration of immunity is likely to be short ( $< 4$  years) across a plausible range of  $\mathcal{R}_0$  ( $< 6$ ). We were also able to obtain

290 a plausible range of susceptible replenishment rates for each pathogen (Figure 5B),  
 291 but there was a large uncertainty in the estimates for susceptible replenishment rates  
 292 due to a lack of one-to-one correspondence between susceptible replenishment rates  
 293 and pathogen resilience.

## 294 **Pathogen resilience determines sensitivity to stochastic perturbations**

295 Beyond the pandemic perturbations, we hypothesized host-pathogen systems to experience continued perturbations of varying degrees from changes in epidemiological conditions, such as human behavior, climate, and viral evolution. These perturbations can also arise from demographic stochasticity, which is inherent to any ecological systems. Here, we used a seasonally unforced SIRS model with birth/death to explore how resilience of a host-pathogen system determines the sensitivity to perturbations caused by demographic stochasticity (Materials and Methods).

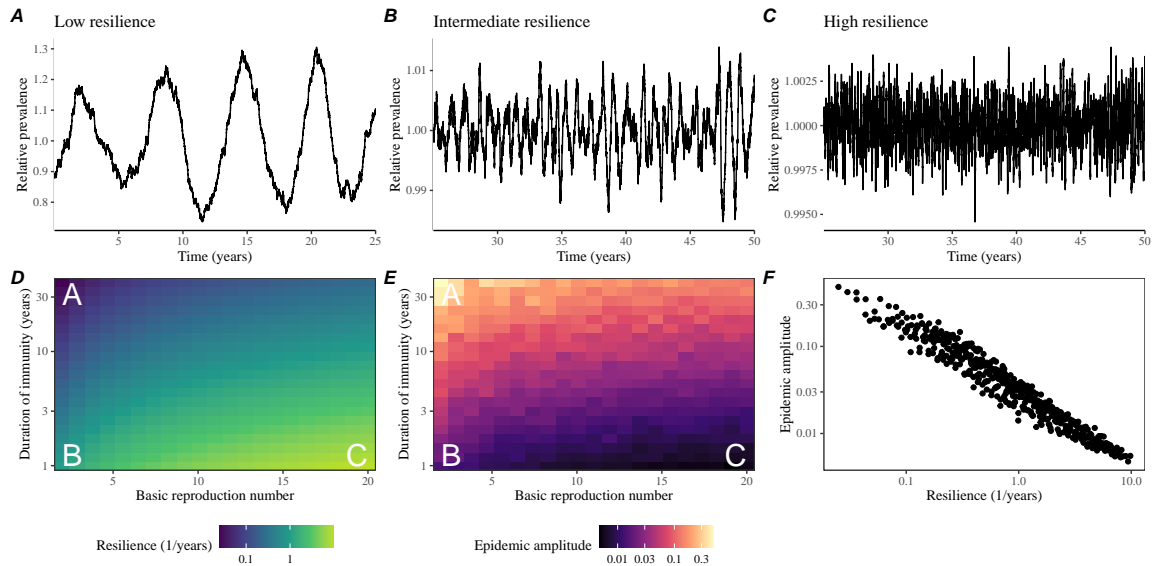


Figure 6: **Linking resilience of a host-pathogen system to its sensitivity to stochastic perturbations.** (A–C) Epidemic trajectories of a stochastic SIRS model across three different resilience values: low, intermediate, and high. The relative prevalence was calculated by dividing infection prevalence by its mean value. (D) Intrinsic resilience of a system as a function of the basic reproduction number  $\mathcal{R}_0$  and the duration of immunity. (E) Epidemic amplitude as a function of the basic reproduction number  $\mathcal{R}_0$  and the duration of immunity. The epidemic amplitude corresponds to  $(\max I - \min I)/(2\bar{I})$ , where  $\bar{I}$  represents the mean prevalence. (F) The relationship between pathogen resilience and epidemic amplitude.

303 We found that resilience of a host-pathogen system determines the amount of  
304 deviation from the deterministic trajectory caused by demographic stochasticity,  
305 with less resilient systems experiencing larger deviations (Figure 6). Notably, less  
306 resilience systems also exhibited slower epidemic cycles (Figure 6A–C). The period-  
307 icity of this epidemic cycle matched those predicted by the intrinsic periodicity of the  
308 system (Supplementary Figure S13) where the intrinsic resilience of the system is in-  
309 versely proportional to its intrinsic periodicity (Supplementary Figure S14). We note  
310 that the intrinsic resilience is not the sole determinant for how sensitive the system is  
311 to stochastic perturbations. For example, the population size and average duration of  
312 infection also affect the amount of deviation from the deterministic trajectory caused  
313 by demographic stochasticity, even though these quantities have little to no impact  
314 on the intrinsic resilience (Supplementary Figure S15). These conclusions were robust  
315 for the seasonally forced SIRS model (Supplementary Figure S16).

## 316 Discussion

317 COVID-19 pandemic interventions caused major disruptions to circulation patterns  
318 of both respiratory and non-respiratory pathogens, adding challenges to predicting  
319 their future dynamics [1, 2, 3, 4]. However, these perturbations offer large-scale natu-  
320 ral experiments for understanding how different pathogens respond to perturbations.  
321 In this study, we showed that pathogen re-emergence patterns following pandemic  
322 perturbations can be characterized through the lens of ecological resilience. We  
323 showed that variation in pathogen resilience can be explained by the differences in  
324 susceptible host dynamics, where faster replenishment of the susceptible pool corre-  
325 sponds to a more resilient host-pathogen system. Finally, we showed that pathogen  
326 resilience also determines the sensitivity to stochastic perturbations.

327 We analyzed case time series of common respiratory infections and norovirus  
328 infections from Canada, Hong Kong, Korea, and the US to estimate their resilience.  
329 Overall, we estimated the resilience of these pathogens to range from 0.4/year to  
330 1.8/year, which is 3–14 times more resilient than prevaccination measles. These  
331 resilience estimates indicate that common respiratory pathogens and norovirus likely  
332 exhibit faster susceptible replenishment and are therefore more persistent, indicating  
333 potential challenges in controlling these pathogens.

334 Based on our resilience estimates, we made phenomenological predictions about  
335 when each pathogen will return to their endemic cycles. For the most part, we  
336 accurately predicted which pathogens should have already returned before the end  
337 of 2024. However, there were two main exceptions (i.e., norovirus in Hong Kong  
338 and rhinovirus/enterovirus in the US), suggesting that these pathogens may be con-  
339 verging to new endemic cycles or experiencing long-term transient behavior. These  
340 changes may reflect changes in surveillance or actual shift in the dynamics, caused  
341 by permanent changes in behavior or population-level immunity. While it may seem  
342 unlikely that permanent changes in behavior would only affect a few pathogens and

343 not others, we cannot rule out this possibility given differences in the observed mean  
344 age of infections and therefore the differences in age groups that primarily drive  
345 transmission [22, 23]. Differences in the mode of transmission between respiratory  
346 vs gastrointestinal pathogens may also contribute to the differences in responses to  
347 pandemic perturbations.

348 For almost half of the pathogens we considered, we predicted that their return  
349 to original epidemic patterns is imminent. We will need a few more years of data  
350 to test whether these pathogens will eventually return to their original dynamics or  
351 eventually converge to a different attractor. We also cannot rule out the possibility  
352 that some pathogens may exhibit long-term transient behaviors following pandemic  
353 perturbations. Overall, these observations echo earlier studies that highlighted the  
354 long-lasting impact of pandemic perturbations [8, 24, 25, 4].

355 We showed that susceptible host dynamics shape pathogen resilience, where faster  
356 replenishment of the susceptible population causes the pathogen to be more resilient.  
357 For simplicity, we focus on waning immunity and birth as the main drivers of the  
358 susceptible host dynamics but other mechanisms can also contribute to the replenish-  
359 ment of the susceptible population. In particular, pathogen evolution, especially the  
360 emergence of antigenically novel strains, can cause effective waning of immunity in  
361 the population; therefore, we hypothesize that the rate of antigenic evolution is likely  
362 a key feature of pathogen resilience. Future studies should explore the relationship  
363 between the rate of evolution and resilience for antigenically evolving pathogens.

364 Quantifying pathogen resilience also offers novel approaches to validating population-  
365 level epidemiological models. So far, most model validation in infectious disease ecol-  
366 ogy is based on the ability of a model to reproduce the observed epidemic dynamics  
367 and to predict future dynamics [26, 27, 28, 29, 30]. However, many models can  
368 perform similarly under these criteria. For example, two major RSV models have  
369 been proposed to explain biennial epidemic patterns: (1) a stage- and age-structured  
370 model that allows disease severity to vary with number of past infections and age of  
371 infection [28] and (2) a pathogen-interaction model that accounts for cross immunity  
372 between RSV and human metapneumovirus [27]. Since both models can accurately  
373 reproduce the observed epidemic patterns, standard criteria for model validation  
374 do not allow us to distinguish between these two models from population-level data  
375 alone. Instead, it would be possible to measure the empirical resilience of each model  
376 by simulating various perturbations and comparing the simulations to estimates of  
377 empirical resilience from data, using pandemic perturbations as a reference.

378 There are several limitations to our work. First, we did not extensively explore  
379 other approaches to reconstructing the attractor. Recent studies showed that more  
380 sophisticated approaches, such as using non-uniform embedding, can provide more  
381 robust reconstruction for noisy data [21]. In the context of causal inference, choices  
382 about embedding can have major impact on the resulting inference [31]. Our re-  
383 silience estimates are likely overly confident given a lack of uncertainties in attractor  
384 reconstruction as well as the simplicity of our statistical framework. Nonetheless,  
385 as illustrated in our sensitivity analyses, inferences about pathogen resilience in our

386 SIRS model appear to be robust to decisions about embedding lags and dimensions—  
387 this is because tracking the rate at which the system approaches the attractor is likely  
388 a much simpler problem than making inferences about causal directionality. Short  
389 pre-pandemic time series also limit our ability to accurately reconstruct the attrac-  
390 tor and contribute to the crudeness of our resilience estimates; although this is less  
391 likely a problem for respiratory pathogens that are strongly annual, our attractor  
392 reconstruction may be inaccurate for those exhibiting multi-annual cycles, such as  
393 adenovirus in Hong Kong and Korea. Our framework also do not allow us to distin-  
394 guish whether a system has settled to a new attractor or is experiencing long-term  
395 transient behavior. Uncertainties in pathogen dynamics due to changes in testing  
396 patterns further contribute to the crudeness of our resilience estimates. Despite these  
397 limitations, our qualitative prediction that common respiratory pathogens are more  
398 resilient than prevaccination measles is also likely to be robust, given how rapid many  
399 respiratory pathogens returned to their original cycles following pandemic perturba-  
400 tions.

401 Predicting the impact of anthropogenic changes on infectious disease dynamics  
402 is a fundamental aim of infectious disease research in a rapidly changing world. Our  
403 study illustrates that how a host-pathogen system responds to both small and large  
404 perturbations is largely predictable through the lens of ecological resilience. In par-  
405 ticular, quantifying the resilience of a host-pathogen system offers a unique insight  
406 into questions about endemic pathogens' responses to pandemic perturbations, in-  
407 cluding whether some pathogens will exhibit long-lasting impact from the pandemic  
408 perturbation or not. More broadly, a detailed understanding of the determinants of  
409 pathogen resilience can provide deeper understanding of pathogen persistence.

## 410 Materials and Methods

### 411 Data

412 We gathered time series on respiratory infections from Canada, Hong Kong, Korea,  
413 and United States (US). As a reference, we also included time series data on norovirus  
414 infections when available. In contrast to respiratory pathogens, we hypothesized  
415 gastrointestinal viruses, such as norovirus, to be differently affected by pandemic  
416 perturbations.

417 Weekly time series of respiratory infection cases in Canada came from a publicly  
418 available website by the Respiratory Virus Detection Surveillance System, which  
419 collects data from select laboratories across Canada [32]. Weekly time series of  
420 respiratory infection cases in Hong Kong came from a publicly available website by  
421 the Centre for Health Protection, Department of Health [33, 34]. Weekly time series  
422 of acute respiratory infection cases in Korea came from a publicly available website  
423 by the Korea Disease Control and Prevention Agency [35]. Finally, weekly time series  
424 of respiratory infection cases in the US were obtained from the National Respiratory  
425 and Enteric Virus Surveillance System. Time series on number of tests were also

426 available in Canada, Hong Kong, and the US, but not in Korea. [SWP: Not sure  
427 how to cite NREVSS data because we got it by emailing them...]

## 428 Data processing

429 For all time series, we rounded every year to 52 weeks by taking the average number  
430 of cases and tests between the 52nd and 53rd week. We also rescale all time series to  
431 account for changes in testing patterns, which were then used for the actual analysis.

432 For Canada, an increase in testing was observed from 2013 to 2024 (Supplemen-  
433 tary Figure S15). To account for this increase, we calculated a 2 year moving average  
434 for the number of tests for each pathogen, which we used as a proxy for testing effort.  
435 Then, we divided the smoothed testing patterns by the smoothed value at the final  
436 week such that the testing effort has a maximum of 1. We then divided weekly cases  
437 by the testing effort to obtain a scaled case time series. A similar approach was used  
438 earlier for an analysis of RSV time series in the US to account for changes in testing  
439 patterns [28].

440 For Hong Kong, we applied the same scaling procedure to the time series as we  
441 did for Canada. In this case, we only adjusted for testing efforts up to the end of 2019  
442 because there was a major reduction in testing for common respiratory pathogens  
443 since 2020 (Supplementary Figure S17).

444 For Korea, while we did not have information on testing, the reported number  
445 of respiratory infections consistently increased from 2013 to the end of 2019, which  
446 we interpreted as changes in testing patterns (Supplementary Figure S18). Since  
447 we did not have testing numbers, we used the weekly sum of all acute respiratory  
448 viral infection cases as a proxy for testing, which were further smoothed with moving  
449 averaged and scaled to have a maximum of 1. For Korea, we also only adjusted for  
450 testing efforts up to the end of 2019.

451 In the US, there has been a large increase in testing against some respiratory  
452 pathogens, especially RSV, which could not be corrected for through simple scaling  
453 (Supplementary Figure S19). Instead, we derived an incidence proxy by multiply-  
454 ing the test positivity with influenza-like illness positivity, which was taken from  
455 <https://gis.cdc.gov/grasp/fluview/fluportaldashboard.html>. This method  
456 of estimating an incidence proxy has been recently applied in the analysis of seasonal  
457 coronaviruses [7] and *Mycoplasma pneumoniae* infections [4]. Detailed assumptions  
458 and justifications are provided in [36].

## 459 Data summary

460 To make qualitative comparisons between pre- and post-perturbation dynamics of  
461 respiratory pathogen circulation patterns, we calculate the mean seasonal patterns  
462 using time series of either rescaled cases or incidence proxy estimates before 2020. We  
463 do so by taking the mean value in each week across all years before 2020. Confidence  
464 intervals around the means are calculated using a simple t test.

465 **Estimating pathogen resilience**

466 In order to measure pathogen resilience from surveillance data, we first reconstructed  
 467 the empirical pre-pandemic attractor of the system using Takens' embedding theorem  
 468 [17]. Specifically, for a given pathogen, we took the pre-pandemic (before 2020)  
 469 case time series  $C(t)$  and reconstruct the attractor using delayed embedding with a  
 470 uniform delay of  $\tau$  and dimension  $M$ :

$$X_{\tau,m}(t) = \langle \log(C(t) + 1), \log(C(t - \tau) + 1), \dots, \log(C(t - (M-1)\tau) + 1) \rangle. \quad (2)$$

471 Here, the delay  $\tau$  was determined by calculating the autocorrelation of the logged  
 472 pre-pandemic time series and asking when the autocorrelation crosses 0 for the first  
 473 time [21]; a typical delay for an annual outbreak is around 13 weeks.

474 Then, for a given delay  $\tau$ , we determined the embedding dimension  $M$  using the  
 475 false nearest neighbors approach [20, 21]. To do so, we started with an embedding  
 476 dimension  $e$  and construct a set of points  $A_{\tau,e} = \{X_{\tau,e}(t) | t < 2020\}$ . Then, for  
 477 each point  $X_{\tau,e}(t)$ , we determined the nearest neighbor from the set  $A_{\tau,e}$ , which we  
 478 denote  $X_{\tau,e}(t_{nn})$  for  $t \neq t_{nn}$ . Then, if the distance between these two points on  $e+1$   
 479 dimension,  $D_{\tau,e+1}(t) = \|X_{\tau,e+1}(t_{nn}) - X_{\tau,e+1}(t)\|_2$ , is larger than their distance on  
 480  $e$  dimension,  $D_{\tau,e}(t) = \|X_{\tau,e}(t_{nn}) - X_{\tau,e}(t)\|_2$ , these two points are deemed to be  
 481 false nearest neighbors; specifically, we used a threshold  $R$  for the ratio between  
 482 two distances  $D_{\tau,e+1}(t)/D_{\tau,e}(t)$  to determine false nearest neighbors. For the main  
 483 analysis, we used  $R = 10$ , which was chosen from a sensitivity analysis against  
 484 simulated data (Supplementary Text). Once we determined the embedding lag  $\tau$   
 485 and dimension  $M$ , we apply the embedding to the entire time series and calculate  
 486 the nearest neighbor distance against the attractor  $A_{\tau,M}$  to obtain a time series of  
 487 distance from the attractor  $D_{\tau,M}(t)$ .

488 From a time series of distances from the attractor, we estimated pathogen re-  
 489 silience by fitting a linear regression to an appropriate window. To automatically se-  
 490 lect the fitting window, we began by smoothing the distance time series using locally  
 491 estimated scatterplot smoothing (LOESS) to obtain  $\hat{D}_{\tau,M}(t)$ , where the smoothing  
 492 is performed on a log scale and exponentiated afterwards. Then, we determined  
 493 threshold values ( $T_{\text{start}}$  and  $T_{\text{end}}$ ) for the smoothed distances and choose the fitting  
 494 window based on when  $\hat{D}_{\tau,M}(t)$  crosses these threshold values for the first time.  
 495 These thresholds were determined by first calculating maximum distance,

$$\max \hat{D} = \max \hat{D}_{\tau,M}(t), \quad (3)$$

496 and mean pre-pandemic distance,

$$\hat{D}_{\text{mean}} = \frac{1}{N_{t<2020}} \sum_{t<2020} \hat{D}_{\tau,M}(t), \quad (4)$$

497 as a reference, and then dividing their ratios into  $K$  equal bins:

$$T_{\text{start}} = \hat{D}_{\text{mean}} \times \left( \frac{\max \hat{D}}{\hat{D}_{\text{mean}}} \right)^{(K-a)/K} \quad (5)$$

$$T_{\text{end}} = \hat{D}_{\text{mean}} \times \left( \frac{\max \hat{D}}{\hat{D}_{\text{mean}}} \right)^{a/K} \quad (6)$$

498 where  $a$  represents the truncation threshold. This allows us to discard the initial  
 499 period during which the distance increases (from the introduction of intervention  
 500 measures) and the final period during which the distance plateaus (as the system  
 501 reaches an attractor). The fitting window is determined based on when the smoothed  
 502 distance  $\hat{D}_{\tau,M}(t)$  crosses these threshold values for the first time; then, we fit a  
 503 linear regression to logged (unsmoothed) distances  $\log D_{\tau,M}(t)$  using that window.  
 504 Alongside the threshold  $R$  for the false nearest neighbors approach, we tested optimal  
 505 choices for  $K$  and  $a$  values using simulations (Supplementary Text). We used  $K = 19$   
 506 and  $a = 2$  throughout the paper based on the simulation results.

## 507 Mathematical modeling

508 Throughout the paper, we use a series of mathematical models to illustrate the  
 509 concept of pathogen resilience and to understand the determinants of pathogen re-  
 510 silience. In general, the intrinsic resilience for a given system is given by the largest  
 511 real part of the eigenvalues of the linearized system at endemic equilibrium. Here, we  
 512 focus on the SIRS model with demography (birth and death) and present the details  
 513 of other models in Supplementary Text. The SIRS (Susceptible-Infected-Recovered-  
 514 Susceptible) model is the simplest model that allows for waning of immunity, where  
 515 recovered (immune) individuals are assumed to become fully susceptible after an  
 516 average of  $1/\delta$  time period. The dynamics of the SIRS model is described by the  
 517 following set of differential equations:

$$\frac{dS}{dt} = \mu - \beta(t)SI - \mu S + \delta R \quad (7)$$

$$\frac{dI}{dt} = \beta(t)SI - (\gamma + \mu)I \quad (8)$$

$$\frac{dR}{dt} = \gamma I - (\delta + \mu)R \quad (9)$$

$$(10)$$

518 where  $\mu$  represents the birth/death rate,  $\beta(t)$  represents the time-varying trans-  
 519 mission rate, and  $\gamma$  represents the recovery rate. The basic reproduction number  
 520  $\mathcal{R}_0(t) = \beta(t)/(\gamma + \mu)$  is defined as the average number of secondary infections that  
 521 a single infected individual would cause in a fully susceptible population at time  $t$   
 522 and measures the intrinsic transmissibility of a pathogen.

523 When we first introduced the idea of pathogen resilience (Figure 2), we imposed  
 524 sinusoidal changes to the transmission rate to account for seasonal transmission:

$$\beta(t) = b_1(1 + \theta \cos(2\pi(t - \phi)))\alpha(t), \quad (11)$$

525 where  $b_1$  represents the baseline transmission rate,  $\theta$  represents the seasonal amplitude,  
 526 and  $\phi$  represents the seasonal offset term. Here, we also introduced an extra  
 527 multiplicative term  $\alpha(t)$  to account for the impact of pandemic perturbations, where  
 528  $\alpha(t) < 1$  indicates transmission reduction. Figure 2A and 2B were generated assuming  
 529  $b_1 = 3 \times (365/7 + 1/50)/\text{years}$ ,  $\theta = 0.2$ ,  $\phi = 0$ ,  $\mu = 1/50/\text{years}$ ,  $\gamma = 365/7/\text{years}$ ,  
 530 and  $\delta = 1/2/\text{years}$ . In Figure 2A, we imposed a 50% transmission reduction for 6  
 531 months from 2020:

$$\alpha(t) = \begin{cases} 0.5 & 2020 \leq t < 2020.5 \\ 1 & \text{otherwise} \end{cases} \quad (12)$$

532 In Figure 2B, we imposed a 50% transmission reduction for 6 months from 2020 and  
 533 a permanent 10% reduction onward:

$$\alpha(t) = \begin{cases} 1 & t < 2020 \\ 0.5 & 2020 \leq t < 2020.5 \\ 0.9 & 2020.5 \leq t \end{cases} \quad (13)$$

534 In both scenarios, we simulated the SIRS model from the following initial conditions  
 535 ( $S(0) = 1/\mathcal{R}_0$ ,  $I(0) = 1 \times 10^{-6}$ , and  $R(0) = 1 - S(0) - I(0)$ ) from 1900 until 2030.

536 To measure the empirical resilience of the SIRS model (Figure 2C and 2F), we  
 537 computed the normalized distance between post-intervention susceptible and logged  
 538 infected proportions and their corresponding unperturbed values at the same time:

$$\sqrt{\left(\frac{S(t) - S_{\text{unperturbed}}(t)}{\sigma_S}\right)^2 + \left(\frac{\log I(t) - \log I_{\text{unperturbed}}(t)}{\sigma_{\log I}}\right)^2}, \quad (14)$$

539 where  $\sigma_S$  and  $\sigma_{\log I}$  represent the standard deviation in the unperturbed susceptible  
 540 and logged infected proportions. The unperturbed values were obtained by simulating  
 541 the same SIRS model without pandemic perturbations ( $\alpha = 1$ ). We normalized  
 542 the differences in susceptible and logged infected proportions to allow both quantities  
 543 to equally contribute to the changes in distance from the attractor. We used logged  
 544 prevalence, instead of absolute prevalence, in order to capture epidemic dynamics  
 545 in deep troughs during the intervention period. In Supplementary Materials, we  
 546 also compared how the degree of seasonal transmission affects empirical resilience  
 547 by varying  $\theta$  from 0 to 0.4; when we assumed no seasonality ( $\theta = 0$ ), we did not  
 548 normalize the distance because the standard deviation of pre-intervention dynamics  
 549 are zero.

550 We used the SIRS model to understand how underlying epidemiological parameters  
 551 affect pathogen resilience and link this relationship to underlying susceptible  
 552 host dynamics. For the simple SIRS model without seasonal transmission ( $\theta = 0$ ),  
 553 the intrinsic resilience corresponds to

$$-\frac{\text{Re}(\lambda)}{2} = \frac{\delta + \beta I^* + \mu}{2}. \quad (15)$$

554 Here,  $I^*$  represents the prevalence at endemic equilibrium:

$$I^* = \frac{(\delta + \mu)(\beta - (\gamma + \mu))}{\beta(\delta + \gamma + \mu)}. \quad (16)$$

555 The susceptible replenishment rate is given by

$$S_{\text{replenish}} = \frac{\mu + \delta R}{S^*}, \quad (17)$$

556 where  $S^* = 1/\mathcal{R}_0$  represents the equilibrium proportion of susceptible individuals.  
557 We varied the basic reproduction number  $\mathcal{R}_0$  between 1.1 to 6 and the average  
558 duration of immunity  $1/\delta$  between 2 to 4 years, and computed these two quantities.  
559 In doing so, we fixed all other parameters:  $\mu = 1/80/\text{years}$  and  $\gamma = 365/7/\text{years}$ .  
560 When infection provides a life-long immunity ( $\delta = 0$ ), the intrinsic resilience is  
561 inversely proportional to the susceptible replenishment rate:

$$-\frac{\text{Re}(\lambda)}{2} = \frac{\mu}{2S^*} = \frac{S_{\text{replenish}}}{2}. \quad (18)$$

562 Finally, we used a seasonally unforced stochastic SIRS model without demog-  
563 raphy to understand how pathogen resilience affects sensitivity of the system to  
564 demographic stochasticity (see Supplementary Text for the details of the stochastic  
565 SIRS model). By varying the basic reproduction number  $\mathcal{R}_0$  between 2 to 20 and  
566 the average duration of immunity  $1/\delta$  between 1 to 40 years, we ran the the SIRS  
567 model for 100 years and computed the epidemic amplitude, which we defined as  
568  $(\max I - \min I)/(2\bar{I})$ . Each simulation began from the equilibrium, and we trun-  
569 cated initial 25 years before computing the epidemic amplitude. In doing so, we  
570 assumed  $\gamma = 365/7/\text{years}$  and fixed the population size to 1 billion to prevent any  
571 fadeouts. We also considered using a seasonally forced stochastic SIRS model with-  
572 out demography, assuming an amplitude of seasonal forcing of 0.04; in this case,  
573 we computed the relative epidemic amplitude by comparing the deterministic and  
574 stochastic trajectories (Supplementary Materials).

## 575 Data availability

576 All data and code are stored in a publicly available GitHub repository (<https://github.com/cobeylab/return-time>).  
577

## 578 Funding

579 S.W.P. is a Peter and Carmen Lucia Buck Foundation Awardee of the Life Sciences  
580 Research Foundation.

581 **Supplementary Text**

582 **Resilience of a stage-structured system.**

583 In Figure 2G–I, we used a more realistic, stage-structured model to illustrate how  
 584 transient phenomena can cause the system to slow down. Specifically, we used the  
 585 stage-structured RSV model proposed by [28], which assumes that subsequent rein-  
 586 fections cause an individual to become less susceptible and transmissible than previ-  
 587 ous infections. The model dynamics can be described as follows:

$$\frac{dM}{dt} = \mu - (\omega + \mu)M \quad (S1)$$

$$\frac{dS_0}{dt} = \omega M - (\lambda(t) + \mu)S_0 \quad (S2)$$

$$\frac{dI_1}{dt} = \lambda(t)S_0 - (\gamma_1 + \mu)I_1 \quad (S3)$$

$$\frac{dS_1}{dt} = \gamma_1 I_1 - (\sigma_1 \lambda(t) + \mu)S_1 \quad (S4)$$

$$\frac{dI_2}{dt} = \sigma_1 \lambda(t)S_1 - (\gamma_2 + \mu)I_2 \quad (S5)$$

$$\frac{dS_2}{dt} = \gamma_2 I_2 - (\sigma_2 \lambda(t) + \mu)S_2 \quad (S6)$$

$$\frac{dI_3}{dt} = \sigma_2 \lambda(t)S_2 - (\gamma_3 + \mu)I_3 \quad (S7)$$

$$\frac{dS_3}{dt} = \gamma_3 I_3 - (\sigma_3 \lambda(t) + \mu)S_3 + \gamma_4 I_4 \quad (S8)$$

$$\frac{dI_4}{dt} = \sigma_3 \lambda(t)S_3 - (\gamma_4 + \mu)I_4 \quad (S9)$$

(S10)

588 where  $M$  represents the proportion of individuals who are maternally immune;  $S_i$   
 589 represents the proportion of individuals who are susceptible after  $i$  prior infections;  $I_i$   
 590 represents the proportion of individuals who are currently (re)-infected with their  $i$ -th  
 591 infection;  $\mu$  represents the birth and death rates;  $1/\omega$  represents the mean duration  
 592 of maternal immunity;  $1/\gamma_i$  represents the mean duration of infection;  $\lambda(t)$  represents  
 593 the force of infection; and  $\sigma_i$  represents the reduction in susceptibility for the  $i$ -th  
 594 reinfection. The force of infection is modeled using a sinusoidal function:

$$\beta(t) = b_1(1 + \theta \cos(2\pi(t - \phi)))\alpha(t) \quad (S11)$$

$$\lambda(t) = \beta(I_1 + \rho_1 I_2 + \rho_2(I_3 + I_4)), \quad (S12)$$

595 where  $b_1$  represents the baseline transmission rate;  $\theta$  represents the seasonal ampli-  
 596 tude;  $\phi$  represents the seasonal offset term;  $\alpha(t)$  represents the intervention effect;  
 597 and  $\rho_i$  represents the impact of immunity on transmission reduction. We used the

598 following parameters to simulate the impact of interventions on epidemic dynam-  
 599 ics [28]:  $b_1 = 9 \times (365/10 + 1/80)/\text{years}$ ,  $\theta = 0.2$ ,  $\phi = -0.1$ ,  $\omega = 365/112/\text{years}$ ,  
 600  $\gamma_1 = 365/10/\text{years}$ ,  $\gamma_2 = 365/7/\text{years}$ ,  $\gamma_3 = 365/5/\text{years}$ ,  $\sigma_1 = 0.76$ ,  $\sigma_2 = 0.6$ ,  
 601  $\sigma_3 = 0.4$ ,  $\rho_1 = 0.75$ ,  $\rho_2 = 0.51$ , and  $\mu = 1/80/\text{years}$ . We assumed a 50% transmis-  
 602 sion reduction for 6 months from 2020:

$$\alpha(t) = \begin{cases} 0.5 & 2020 \leq t < 2020.5 \\ 1 & \text{otherwise} \end{cases} \quad (\text{S13})$$

603 The model was simulated from 1900 to 2030 using the following initial conditions:  
 604  $M = 0$ ,  $S_0 = 1/\mathcal{R}_0 - I_1$ ,  $I_1 = 1 \times 10^{-6}$ ,  $S_1 = 1 - 1/\mathcal{R}_0$ ,  $I_2 = 0$ ,  $S_2 = 0$ ,  $I_3 = 0$ ,  
 605  $S_3 = 0$ , and  $I_4 = 0$ . For the phase plane analysis (Figure 2H) and distance analysis  
 606 (Figure 2I), we relied on the average susceptibility,

$$\bar{S} = S_0 + \sigma_1 S_1 + \sigma_2 S_2 + \sigma_3 S_3, \quad (\text{S14})$$

607 and total prevalence,

$$I_{\text{total}} = I_1 + I_2 + I_3 + I_4. \quad (\text{S15})$$

608 These quantities were used to compute the normalized distance from the attractor,  
 609 as described in the main text.

## 610 Resilience of a multistrain system.

611 We used a simple two-strain model to show that a multistrain host-pathogen system  
 612 that is coupled through cross immunity can be described by a single resilience value.  
 613 The model dynamics can be described as follows [27]:

$$\frac{dS}{dt} = \mu - \mu S - (\lambda_1 + \lambda_2)S + \rho_1 R_1 + \rho_2 R_2 \quad (\text{S16})$$

$$\frac{dI_1}{dt} = \lambda_1 S - (\gamma_1 + \mu)I_1 \quad (\text{S17})$$

$$\frac{dI_2}{dt} = \lambda_2 S - (\gamma_2 + \mu)I_2 \quad (\text{S18})$$

$$\frac{dR_1}{dt} = \gamma_1 I_1 - \lambda_2 \epsilon_{21} R_1 - \rho_1 R_1 + \rho_2 R - \mu R_1 \quad (\text{S19})$$

$$\frac{dR_2}{dt} = \gamma_2 I_2 - \lambda_1 \epsilon_{12} R_2 - \rho_2 R_2 + \rho_1 R - \mu R_2 \quad (\text{S20})$$

$$\frac{dJ_1}{dt} = \lambda_1 \epsilon_{12} R_2 - (\gamma_1 + \mu)J_1 \quad (\text{S21})$$

$$\frac{dJ_2}{dt} = \lambda_2 \epsilon_{21} R_1 - (\gamma_2 + \mu)J_2 \quad (\text{S22})$$

$$\frac{dR}{dt} = \gamma_1 J_1 + \gamma_2 J_2 - \rho_1 R - \rho_2 R - \mu R \quad (\text{S23})$$

614 where  $S$  represents the proportion of individuals who are fully susceptible to infections  
 615 by both strains;  $I_1$  represents the proportion of individuals who are infected with strain 1 without prior immunity;  $I_2$  represents the proportion of individuals who are infected with strain 2 without prior immunity;  $R_1$  represents the proportion of individuals who are fully immune against strain 1 and partially susceptible to reinfection by strain 2;  $R_2$  represents the proportion of individuals who are fully immune against strain 2 and partially susceptible to reinfection by strain 1;  $J_1$  represents the proportion of individuals who are infected with strain 1 with prior immunity against strain 2;  $J_2$  represents the proportion of individuals who are infected with strain 2 with prior immunity against strain 1;  $R$  represents the proportion of individuals who are immune to infections from both strains;  $\mu$  represents the birth/death rate;  $\lambda_1$  and  $\lambda_2$  represent the force of infection from strains 1 and 2, respectively;  $\rho_1$  and  $\rho_2$  represent the waning immunity rate;  $\gamma_1$  and  $\gamma_2$  represent the recovery rate;  $\epsilon_{12}$  and  $\epsilon_{21}$  represent the susceptibility to reinfection with strains 2 and 1, respectively, given prior immunity from infection with strains 1 and 2, respectively. The force of infection is modeled as follows:

$$\beta_1 = b_1(1 + \theta_1 \sin(2\pi(t - \phi_1)))\alpha(t) \quad (\text{S24})$$

$$\beta_2 = b_2(1 + \theta_2 \sin(2\pi(t - \phi_2)))\alpha(t) \quad (\text{S25})$$

$$\lambda_1 = \beta_1(I_1 + J_1) \quad (\text{S26})$$

$$\lambda_2 = \beta_2(I_2 + J_2) \quad (\text{S27})$$

630 In Supplementary Figures S2–S4, we assumed the following parameters:  $b_1 = 2 \times$   
 631  $52/\text{years}$ ,  $b_2 = 4 \times 52/\text{years}$ ,  $\phi_1 = \phi_2 = 0$ ,  $\epsilon_{12} = 0.9$ ,  $\epsilon_{21} = 0.5$ ,  $\gamma_1 = \gamma_2 = 52/\text{years}$ ,  
 632  $\rho_1 = \rho_2 = 1/\text{years}$ , and  $\mu = 1/70/\text{years}$ . For all simulations, we assumed a 50%  
 633 transmission reduction for 6 months from 2020:

$$\alpha(t) = \begin{cases} 0.5 & 2020 \leq t < 2020.5 \\ 1 & \text{otherwise} \end{cases} \quad (\text{S28})$$

634 The seasonal amplitude  $\theta$  is varied from 0 to 0.4. All simulations were ran from 1900  
 635 to 2030 with following initial conditions:  $S(0) = 1 - 2 \times 10^{-6}$ ,  $I_1(0) = 1 \times 10^{-6}$ ,  
 636  $I_2(0) = 1 \times 10^{-6}$ ,  $R_1(0) = 0$ ,  $R_2(0) = 0$ ,  $J_1(0) = 0$ ,  $J_2(0) = 0$ , and  $R(0) = 0$ .

637 We considered three scenarios for measuring pathogen resilience: (1) we only have  
 638 information about strain 1, (2) we only have information about strain 2, and (3) we  
 639 are unable to distinguish between strains. In the first two scenarios (see panels A–C  
 640 for strain 1 and panels D–F for strain 2), we considered the dynamics of average  
 641 susceptibility for each strain and total prevalence:

$$\bar{S}_1 = S + \epsilon_{12}R_2 \quad (\text{S29})$$

$$\hat{I}_1 = I_1 + J_1 \quad (\text{S30})$$

$$\bar{S}_2 = S + \epsilon_{21}R_1 \quad (\text{S31})$$

$$\hat{I}_2 = I_2 + J_2 \quad (\text{S32})$$

642 In the third scenario (panels G–I), we considered the dynamics of total susceptible  
643 and infected populations:

$$\hat{S} = S + R_2 + R_1 \quad (\text{S33})$$

$$\hat{I} = I_1 + J_1 + I_2 + J_2 \quad (\text{S34})$$

644 These quantities were used to compute the normalized distance from the attractor,  
645 as described in the main text.

## 646 Estimating intrinsic resilience using mechanistic model

647 We tested whether we can reliably estimate the intrinsic resilience of a system by fit-  
648 ting a mechanistic model. Specifically, we simulated case time series from stochastic  
649 SIRS and two-strain models and fitted a simple, deterministic SIRS model using a  
650 Bayesian framework.

651 We simulated the models in discrete time with a daily time step ( $\Delta t = 1$ ),  
652 incorporating demographic stochasticity:

$$\beta(t) = \mathcal{R}_0 \left( 1 + \theta \cos \left( \frac{2\pi t}{364} \right) \right) \alpha(t)(1 - \exp(-\gamma)) \quad (\text{S35})$$

$$\text{FOI}(t) = \beta(t)I(t - \Delta t)/N \quad (\text{S36})$$

$$B(t) \sim \text{Poisson}(\mu N) \quad (\text{S37})$$

$$\Delta S(t) \sim \text{Binom}(S(t - \Delta t), 1 - \exp(-(\text{FOI}(t) + \mu)\Delta t)) \quad (\text{S38})$$

$$N_{SI}(t) \sim \text{Binom}\left(\Delta S(t), \frac{\text{FOI}(t)}{\text{FOI}(t) + \mu}\right) \quad (\text{S39})$$

$$\Delta I(t) \sim \text{Binom}(I(t - \Delta t), 1 - \exp(-(\gamma + \mu)\Delta t)) \quad (\text{S40})$$

$$N_{IR}(t) \sim \text{Binom}\left(\Delta I(t), \frac{\gamma}{\gamma + \mu}\right) \quad (\text{S41})$$

$$\Delta R(t) \sim \text{Binom}(R(t - \Delta t), 1 - \exp(-(\delta + \mu)\Delta t)) \quad (\text{S42})$$

$$N_{RS}(t) \sim \text{Binom}\left(\Delta R(t), \frac{\delta}{\delta + \mu}\right) \quad (\text{S43})$$

$$S(t) = S(t - \Delta t) + N_{RS}(t) + B(t) - \Delta S(t) \quad (\text{S44})$$

$$I(t) = I(t - \Delta t) + N_{SI}(t) - \Delta I(t) \quad (\text{S45})$$

$$R(t) = R(t - \Delta t) + N_{IR}(t) - \Delta R(t) \quad (\text{S46})$$

653 where FOI represent the force of infection;  $N_{ij}$  represent the number of individuals  
654 moving from compartment  $i$  to  $j$  on a given day; and  $B(t)$  represents the number  
655 of new births. We simulated the model on a daily scale—assuming 364 days in a  
656 year so that it can be evenly grouped into 52 weeks—with the following parameters:  
657  $\mathcal{R}_0 = 3$ ,  $\theta = 0.1$ ,  $\gamma = 1/7/\text{days}$ ,  $\delta = 1/(364 \times 2)/\text{days}$ ,  $\mu = 1/(364 \times 50)/\text{days}$ , and  
658  $N = 1 \times 10^8$ . The model was simulated from 1900 to 2030 assuming  $S(0) = N/3$ ,

659  $I(0) = 100$ , and  $R(0) = N - S(0) - I(0)$ . The observed incidence from the model  
660 was then simulated as follows:

$$C(t) = \text{Beta-Binom}(N_{SI}(t), \rho, k), \quad (\text{S47})$$

661 where  $\rho$  represents the reporting probability and  $k$  represents the overdispersion  
662 parameter of beta-binomial distribution. Here, we used the beta-binomial distribution  
663 to account for overdispersion in reporting. We assumed  $\rho = 0.002$  (i.e., 0.2%  
664 probability) and  $k = 1000$ .

665 We used an analogous approach for the two-strain model:

$$\beta_1(t) = b_1 \left( 1 + \theta_1 \cos \left( \frac{2\pi(t - \phi_1)}{364} \right) \right) \alpha(t) \quad (\text{S48})$$

$$\beta_2(t) = b_2 \left( 1 + \theta_2 \cos \left( \frac{2\pi(t - \phi_2)}{364} \right) \right) \alpha(t) \quad (\text{S49})$$

$$\text{FOI}_1(t) = \beta_1(t)(I_1(t - \Delta t) + J_1(t - \Delta t))/N \quad (\text{S50})$$

$$\text{FOI}_2(t) = \beta_2(t)(I_2(t - \Delta t) + J_2(t - \Delta t))/N \quad (\text{S51})$$

$$B(t) \sim \text{Poisson}(\mu N) \quad (\text{S52})$$

$$\Delta S(t) \sim \text{Binom}(S(t - \Delta t), 1 - \exp(-(\text{FOI}_1(t) + \text{FOI}_2(t) + \mu)\Delta t)) \quad (\text{S53})$$

$$N_{SI_1}(t) \sim \text{Binom}\left(\Delta S(t), \frac{\text{FOI}_1(t)}{\text{FOI}_1(t) + \text{FOI}_2(t) + \mu}\right) \quad (\text{S54})$$

$$N_{SI_2}(t) \sim \text{Binom}\left(\Delta S(t), \frac{\text{FOI}_2(t)}{\text{FOI}_1(t) + \text{FOI}_2(t) + \mu}\right) \quad (\text{S55})$$

$$\Delta I_1(t) \sim \text{Binom}(I_1(t - \Delta t), 1 - \exp(-(\gamma_1 + \mu)\Delta t)) \quad (\text{S56})$$

$$N_{I_1 R_1}(t) \sim \text{Binom}\left(\Delta I_1(t), \frac{\gamma_1}{\gamma_1 + \mu}\right) \quad (\text{S57})$$

$$\Delta I_2(t) \sim \text{Binom}(I_2(t - \Delta t), 1 - \exp(-(\gamma_2 + \mu)\Delta t)) \quad (\text{S58})$$

$$N_{I_2 R_2}(t) \sim \text{Binom}\left(\Delta I_2(t), \frac{\gamma_2}{\gamma_2 + \mu}\right) \quad (\text{S59})$$

$$\Delta R_1(t) \sim \text{Binom}(R_1(t - \Delta t), 1 - \exp(-(\epsilon_{21}\text{FOI}_2(t) + \rho_1 + \mu)\Delta t)) \quad (\text{S60})$$

$$N_{R_1 S}(t) \sim \text{Binom}\left(\Delta R_1(t), \frac{\rho_1}{\epsilon_{21}\text{FOI}_2(t) + \rho_1 + \mu}\right) \quad (\text{S61})$$

$$N_{R_1 J_2}(t) \sim \text{Binom}\left(\Delta R_1(t), \frac{\epsilon_{21}\text{FOI}_2(t)}{\epsilon_{21}\text{FOI}_2(t) + \rho_1 + \mu}\right) \quad (\text{S62})$$

$$\Delta R_2(t) \sim \text{Binom}(R_2(t - \Delta t), 1 - \exp(-(\epsilon_{12}\text{FOI}_1(t) + \rho_2 + \mu)\Delta t)) \quad (\text{S63})$$

$$N_{R_2 S}(t) \sim \text{Binom}\left(\Delta R_2(t), \frac{\rho_2}{\epsilon_{12}\text{FOI}_1(t) + \rho_2 + \mu}\right) \quad (\text{S64})$$

$$N_{R_2 J_1}(t) \sim \text{Binom}\left(\Delta R_2(t), \frac{\epsilon_{12}\text{FOI}_1(t)}{\epsilon_{12}\text{FOI}_1(t) + \rho_2 + \mu}\right) \quad (\text{S65})$$

$$\Delta J_1(t) \sim \text{Binom}(J_1(t - \Delta t), 1 - \exp(-(\gamma_1 + \mu)\Delta t)) \quad (\text{S66})$$

$$N_{J_1R}(t) \sim \text{Binom}\left(\Delta J_1(t), \frac{\gamma_1}{\gamma_1 + \mu}\right) \quad (\text{S67})$$

$$\Delta J_2(t) \sim \text{Binom}(J_2(t - \Delta t), 1 - \exp(-(\gamma_2 + \mu)\Delta t)) \quad (\text{S68})$$

$$N_{J_2R}(t) \sim \text{Binom}\left(\Delta J_2(t), \frac{\gamma_2}{\gamma_2 + \mu}\right) \quad (\text{S69})$$

$$\Delta R(t) \sim \text{Binom}(R(t - \Delta t), 1 - \exp(-(\rho_1 + \rho_2 + \mu)\Delta t)) \quad (\text{S70})$$

$$N_{RR_1}(t) \sim \text{Binom}\left(\Delta R(t), \frac{\rho_1}{\rho_1 + \rho_2 + \mu}\right) \quad (\text{S71})$$

$$N_{RR_2}(t) \sim \text{Binom}\left(\Delta R(t), \frac{\rho_2}{\rho_1 + \rho_2 + \mu}\right) \quad (\text{S72})$$

$$S(t) = S(t - \Delta t) - \Delta S(t) + B(t) + N_{R_1S}(t) + N_{R_2S}(t) \quad (\text{S73})$$

$$I_1(t) = I_1(t - \Delta t) - \Delta I_1(t) + N_{SI_1}(t) \quad (\text{S74})$$

$$I_2(t) = I_2(t - \Delta t) - \Delta I_2(t) + N_{SI_2}(t) \quad (\text{S75})$$

$$R_1(t) = R_1(t - \Delta t) - \Delta R_1(t) + N_{I_1R_1}(t) + N_{RR_1}(t) \quad (\text{S76})$$

$$R_2(t) = R_2(t - \Delta t) - \Delta R_2(t) + N_{I_2R_2}(t) + N_{RR_2}(t) \quad (\text{S77})$$

$$J_1(t) = J_1(t - \Delta t) - \Delta J_1(t) + N_{R_2J_1}(t) \quad (\text{S78})$$

$$J_2(t) = J_2(t - \Delta t) - \Delta J_2(t) + N_{R_1J_2}(t) \quad (\text{S79})$$

$$R(t) = R(t - \Delta t) - \Delta R(t) + N_{J_1R}(t) + N_{J_2R}(t) \quad (\text{S80})$$

We simulated the model on a daily scale with previously estimated parameters for the RSV-HMPV interaction [27]:  $b_1 = 1.7/\text{weeks}$ ,  $b_2 = 1.95/\text{weeks}$ ,  $\theta_1 = 0.4$ ,  $\theta_2 = 0.3$ ,  $\phi_1 = 0.005 \times 7/364$ ,  $\phi_2 = 4.99 \times 7/364$ ,  $\epsilon_{12} = 0.92$ ,  $\epsilon_{21} = 0.45$ ,  $\gamma_1 = 1/10/\text{days}$ ,  $\gamma_2 = 1/10/\text{days}$ ,  $\rho_1 = 1/364/\text{days}$ ,  $\rho_2 = 1/364/\text{days}$ ,  $\mu = 1/(70 \times 364)/\text{days}$ , and  $N = 1 \times 10^8$ . The model was simulated from 1900 to 2030 assuming  $S(0) = N - 200$ ,  $I_1(0) = 100$ ,  $I_2(0) = 100$ ,  $R_1(0) = 0$ ,  $R_2(0) = 0$ ,  $J_1(0) = 0$ ,  $J_2(0) = 0$ , and  $R(0) = 0$ . The observed incidence for each strain is then simulated as follows:

$$C_1(t) = \text{Beta-Binom}(N_{SI_1}(t) + N_{R_2J_1}, \rho, k), \quad (\text{S81})$$

$$C_2(t) = \text{Beta-Binom}(N_{SI_2}(t) + N_{R_1J_2}, \rho, k), \quad (\text{S82})$$

where  $\rho$  represents the reporting probability and  $k$  represents the overdispersion parameter of beta-binomial distribution. We assumed  $\rho = 0.002$  (i.e., 0.2% probability) and  $k = 500$ . We also considered the total incidence:  $C_{\text{total}}(t) = C_1(t) + C_2(t)$ .

For both models, we considered a more realistically shaped pandemic perturbation  $\alpha(t)$  to challenge our ability to estimate the intervention effects. Thus, we assumed a 40% transmission reduction for 3 months from March 2020, followed by a 10% transmission reduction for 6 months, 20% transmission reduction for 3 months,

680 and a final return to normal levels:

$$\alpha(t) = \begin{cases} 1 & t < 2020.25 \\ 0.6 & 2020.25 \leq t < 2020.5 \\ 0.9 & 2020.5 \leq t < 2021 \\ 0.8 & 2021 \leq t < 2021.25 \\ 1 & 2021.25 \leq t \end{cases}. \quad (\text{S83})$$

681 For all simulations, we truncated the time series from the beginning of 2014 to the  
682 end of 2023 and aggregate them into weekly cases.

683 To infer intrinsic resilience from time series, we fitted a simple discrete time,  
684 deterministic SIRS model [4]:

$$\Delta t = 1 \text{ week} \quad (\text{S84})$$

$$\text{FOI}(t) = \beta(t)(I(t - \Delta t) + \omega)/N \quad (\text{S85})$$

$$\Delta S(t) = [1 - \exp(-(\text{FOI}(t) + \mu)\Delta t)] S(t - \Delta t) \quad (\text{S86})$$

$$N_{SI}(t) = \frac{\text{FOI}(t)\Delta S(t)}{\text{FOI}(t) + \mu} \quad (\text{S87})$$

$$\Delta I(t) = [1 - \exp(-(\gamma + \mu)\Delta t)] I(t - \Delta t) \quad (\text{S88})$$

$$N_{IR}(t) = \frac{\gamma \Delta I(t)}{\gamma + \mu} \quad (\text{S89})$$

$$\Delta R(t) = [1 - \exp(-(\nu + \mu)\Delta t)] R(t - \Delta t) \quad (\text{S90})$$

$$N_{RS}(t) = \frac{\nu \Delta R(t)}{\nu + \mu} \quad (\text{S91})$$

$$S(t) = S(t - \Delta t) + \mu S - \Delta S(t) + N_{RS}(t) \quad (\text{S92})$$

$$I(t) = I(t - \Delta t) - \Delta I(t) + N_{SI}(t) \quad (\text{S93})$$

$$R(t) = R(t - \Delta t) - \Delta R(t) + N_{IR}(t) \quad (\text{S94})$$

685 where we include an extra term  $\omega$  to account for external infections. Although actual  
686 simulations did not include any external infections, we found that including this term  
687 generally helped with model convergence in previous analyses [4]. The transmission  
688 rate was divided into a seasonal term  $\beta_{\text{seas}}(t)$  (repeated every year) and intervention  
689 term  $\alpha(t)$ , which were estimated jointly:

$$\beta(t) = \beta_{\text{seas}}(t)\alpha(t), \quad (\text{S95})$$

690 where  $\alpha < 1$  corresponds to reduction in transmission due to intervention effects. To  
691 constrain the smoothness of  $\beta_{\text{seas}}(t)$ , we imposed cyclic, random-walk priors:

$$\beta_{\text{seas}}(t) \sim \text{Normal}(\beta_{\text{seas}}(t - 1), \sigma) \quad t = 2 \dots 52 \quad (\text{S96})$$

$$\beta_{\text{seas}}(1) \sim \text{Normal}(\beta_{\text{seas}}(52), \sigma) \quad (\text{S97})$$

692 [SWP: I noticed that I forgot to put a prior on  $\sigma$  so need to re-do this but won't  
 693 change the results.] We fixed  $\alpha(t) = 1$  for all  $t < 2020$  and estimate  $\alpha$  assuming a  
 694 normal prior:

$$\alpha \sim \text{Normal}(1, 0.25). \quad (\text{S98})$$

695 We assumed weakly informative priors on  $\omega$  and  $\nu$ :

$$\omega \sim \text{Normal}(0, 200) \quad (\text{S99})$$

$$\nu \sim \text{Normal}(104, 26) \quad (\text{S100})$$

696 We assumed that the true birth/death rates, population sizes, and recovery rates are  
 697 known. We note, however, that assuming  $\gamma = 1/\text{week}$  actually corresponds to a mean  
 698 simulated infectious period of 1.6 weeks, which is much longer than the true value;  
 699 this approximation allows us to test whether we can still robustly estimate the in-  
 700 trinsic resilience given parameter mis-specification. Initial conditions were estimated  
 701 with following priors:

$$S(0) = Ns(0) \quad (\text{S101})$$

$$I(0) = Ni(0) \quad (\text{S102})$$

$$s(0) \sim \text{Uniform}(0, 1) \quad (\text{S103})$$

$$i(0) \sim \text{Half-Normal}(0, 0.001) \quad (\text{S104})$$

702 Finally, the observation model was specified as follows:

$$\text{Cases}(t) \sim \text{Negative-Binomial}(\rho N_{SI}(t), \phi) \quad (\text{S105})$$

$$\rho \sim \text{Half-Normal}(0, 0.02) \quad (\text{S106})$$

$$\phi \sim \text{Half-Normal}(0, 10) \quad (\text{S107})$$

703 where  $\rho$  represents the reporting probability and  $\phi$  represents the negative binomial  
 704 overdispersion parameter.

705 The model was fitted to four separate time series: (1) incidence time series from  
 706 the SIRS model, (2) incidence time series for strain 1 from the two-strain model,  
 707 (3) incidence time series for strain 2 from the two-strain model, and (4) combined  
 708 incidence time series for strains 1 and 2 from the two-strain model. The model was  
 709 fitted using rstan [37, 38]. The resulting posterior distribution was used to calculate  
 710 the intrinsic resilience of the seasonally unforced system with the same parameters;  
 711 eigenvalues of the discrete-time SIR model were computed by numerically finding  
 712 the equilibrium and calculating the Jacobian matrix.

## 713 Validations for window-selection criteria

714 We used stochastic SIRS simulations to identify optimal parameters for the window-  
 715 selection criteria that we used for the linear regression for estimating empirical re-  
 716 silience. For each simulation, we began by generating a random perturbation  $\alpha(t)$

717 from a random set of parameters. First, we drew the duration of perturbation  $\tau_{\text{npi}}$   
 718 from a uniform distribution between 1 and 2 years. Then, we drew independent  
 719 normal variables  $z_i$  of length  $\lfloor 364\tau_{\text{npi}} \rfloor$  with a standard deviation of 0.02 and took a  
 720 reverse cumulative sum to obtain a realistic shape for the perturbation:

$$x_n = 1 + \sum_{i=n}^{\lfloor 364\tau_{\text{npi}} \rfloor} z_i, \quad n = 1, \dots, \lfloor 364\tau_{\text{npi}} \rfloor. \quad (\text{S108})$$

721 We repeated this random generation process until less than 10% of  $x_n$  exceeds 1—  
 722 this was done to prevent the perturbation  $\alpha(t)$  stays below 1 (and therefore reduce  
 723 transmission) for the most part. Then, we set any values that are above 1 or below 0  
 724 as 1 and 0, respectively. Then, we randomly drew the minimum transmission during  
 725 perturbation  $\alpha_{\min}$  from a uniform distribution between 0.5 and 0.7 and scale  $x_n$  to  
 726 have a minimum of  $\alpha_{\min}$ :

$$x_{\text{scale},n} = \alpha_{\min} + (1 - \alpha_{\min}) \times \frac{x_n - \min x_n}{1 - \min x_n}. \quad (\text{S109})$$

727 This allowed us to simulate a realistically shaped perturbation:

$$\alpha(t) = \begin{cases} 1 & t < 2020 \\ x_{\text{scale},364(t-2020)} & 2020 \leq t < 2020 + \tau_{\text{npi}} \\ 1 & \tau_{\text{npi}} \leq t \end{cases}. \quad (\text{S110})$$

728 Given this perturbation function, we draw  $\mathcal{R}_0$  from a uniform distribution between  
 729 1.5 and 4 and the mean duration of immunity  $1/\delta$  from a uniform distribution be-  
 730 tween 1 and 4. Then, we simulate the stochastic SIRS model from  $S(0) = 10^8/\mathcal{R}_0$   
 731 and  $I(0) = 100$  from 1990 to 2025 and truncate the time series to 2014–2025; if the  
 732 epidemic becomes extinct before the end of simulation, we discard that simulation  
 733 and start over from the perturbation generation step.

734 For each epidemic simulation, we computed the empirical resilience by varying  
 735 the threshold  $R$  for the nearest neighbor approach from 4 to 14 with increments of  
 736 2, the number of divisions  $K$  for the window selection between 8 and 25, and the  
 737 truncation threshold  $a$  for the window selection between 1 to 3; this was done for all  
 738 possible combinations of  $R$ ,  $K$ , and  $a$ . We also compared this with the naive approach  
 739 that uses the entire distance-from-attractor time series, starting from the maximum  
 740 distance to the end of the time series. We repeated this procedure 500 times and  
 741 quantified the correlation between empirical and intrinsic resilience estimates across  
 742 two approaches.

## Supplementary Figures

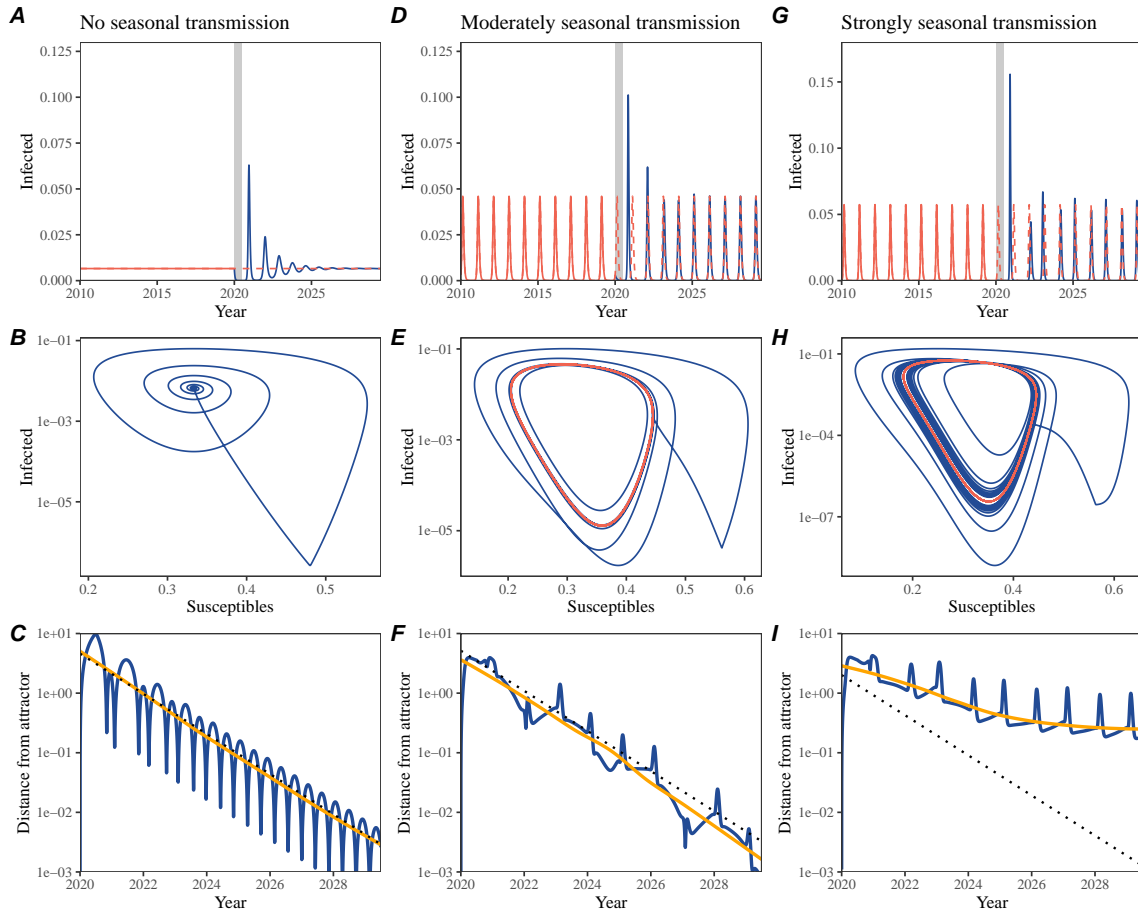


**Figure S1: Impact of seasonal transmission on pathogen resilience.** (A, D, G) Simulated epidemic trajectories using the SIRS model without seasonal forcing (A), with seasonal forcing of amplitude of 0.2 (D), and with seasonal forcing of amplitude of 0.4 (G). Red and blue solid lines represent epidemic dynamics before and after interventions are introduced, respectively. Red dashed lines represent counterfactual epidemic dynamics in the absence of interventions. Gray regions indicate the duration of interventions. (B, E, H) Phase plane representation of the time series in panels A, D, and G alongside the corresponding susceptible host dynamics. Red and blue solid lines represent epidemic trajectories on an SI phase plane before and after interventions are introduced, respectively. (C, F, I) Changes in logged distance from the attractor over time. Blue lines represent the logged distance from the attractor. Orange lines represent the locally estimated scatterplot smoothing (LOESS) fits to the logged distance from the attractor. Dotted lines show the intrinsic resilience of the seasonally unforced system.

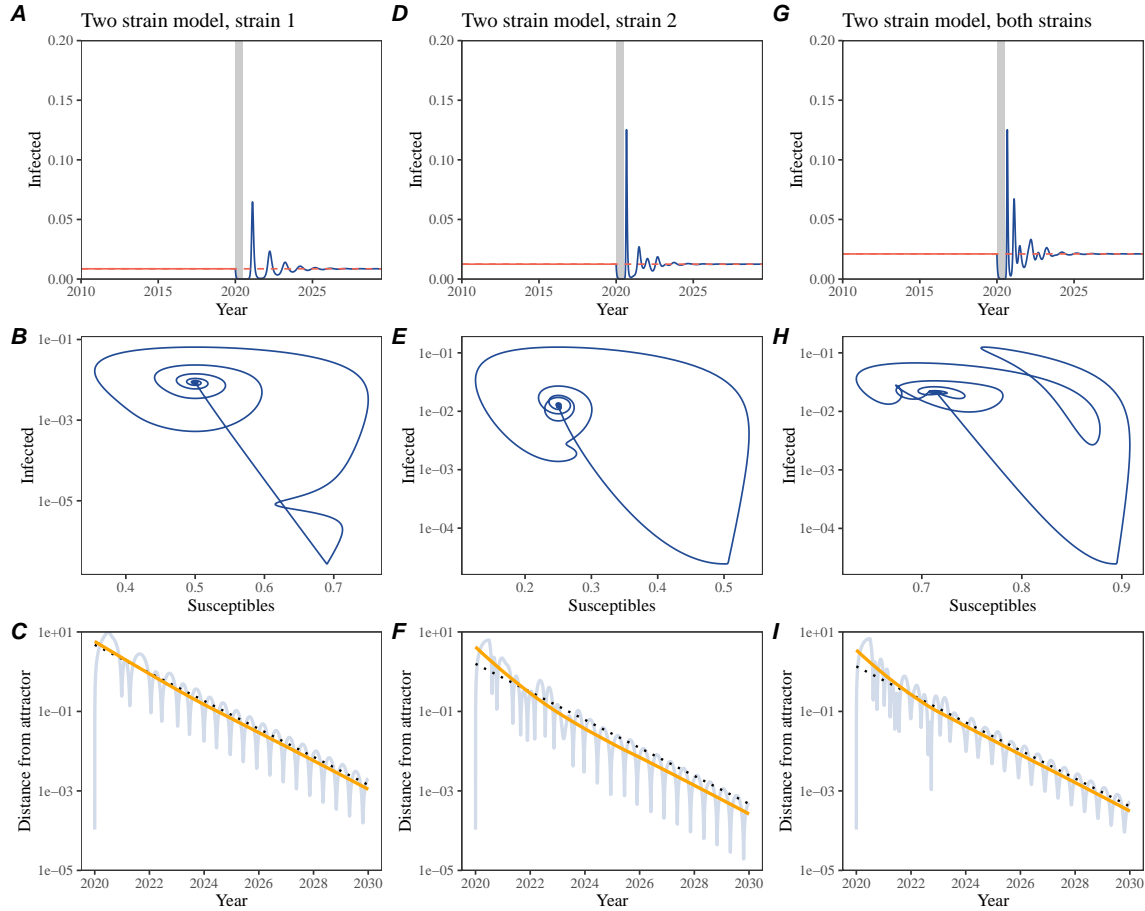


**Figure S2: A simple method to measure pathogen resilience following pandemic perturbations for a two-strain system without seasonal forcing.** (A, D, G) Simulated epidemic trajectories using a multi-strain system without seasonal forcing. Red and blue solid lines represent epidemic dynamics before and after interventions are introduced, respectively. Red dashed lines represent counterfactual epidemic dynamics in the absence of interventions. Gray regions indicate the duration of interventions. (B, E, H) Phase plane representation of the time series in panels A, D, and G alongside the corresponding susceptible host dynamics. Blue solid lines represent epidemic trajectories on an SI phase plane before and after interventions are introduced, respectively. (C, F, I) Changes in logged distance from the attractor over time. Blue lines represent the logged distance from the attractor. Orange lines represent the locally estimated scatterplot smoothing (LOESS) fits to the logged distance from the attractor. Dotted lines show the intrinsic resilience of the seasonally unforced system.

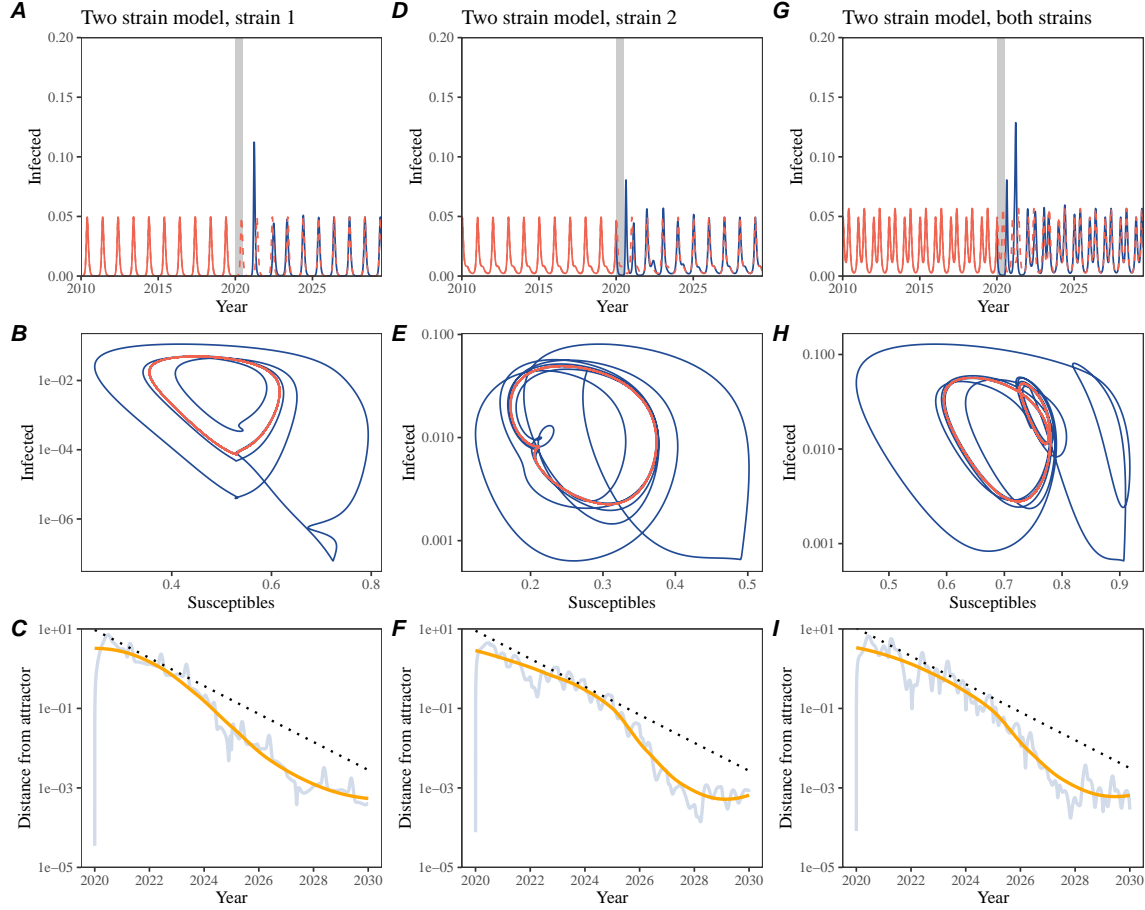


**Figure S3: A simple method to measure pathogen resilience following pandemic perturbations for a two-strain system with seasonal forcing.** (A, D, G) Simulated epidemic trajectories using a two-strain system with seasonal forcing (amplitude of 0.2). In this model, two strains compete through cross immunity. Red and blue solid lines represent epidemic dynamics before and after interventions are introduced, respectively. Red dashed lines represent counterfactual epidemic dynamics in the absence of interventions. Gray regions indicate the duration of interventions. (B, E, H) Phase plane representation of the time series in panels A, D, and G alongside the corresponding susceptible host dynamics. Red and blue solid lines represent epidemic trajectories on an SI phase plane before and after interventions are introduced, respectively. (C, F, I) Changes in logged distance from the attractor over time. Blue lines represent the logged distance from the attractor. Orange lines represent the locally estimated scatterplot smoothing (LOESS) fits to the logged distance from the attractor. Dotted lines show the intrinsic resilience of the seasonally unforced system.

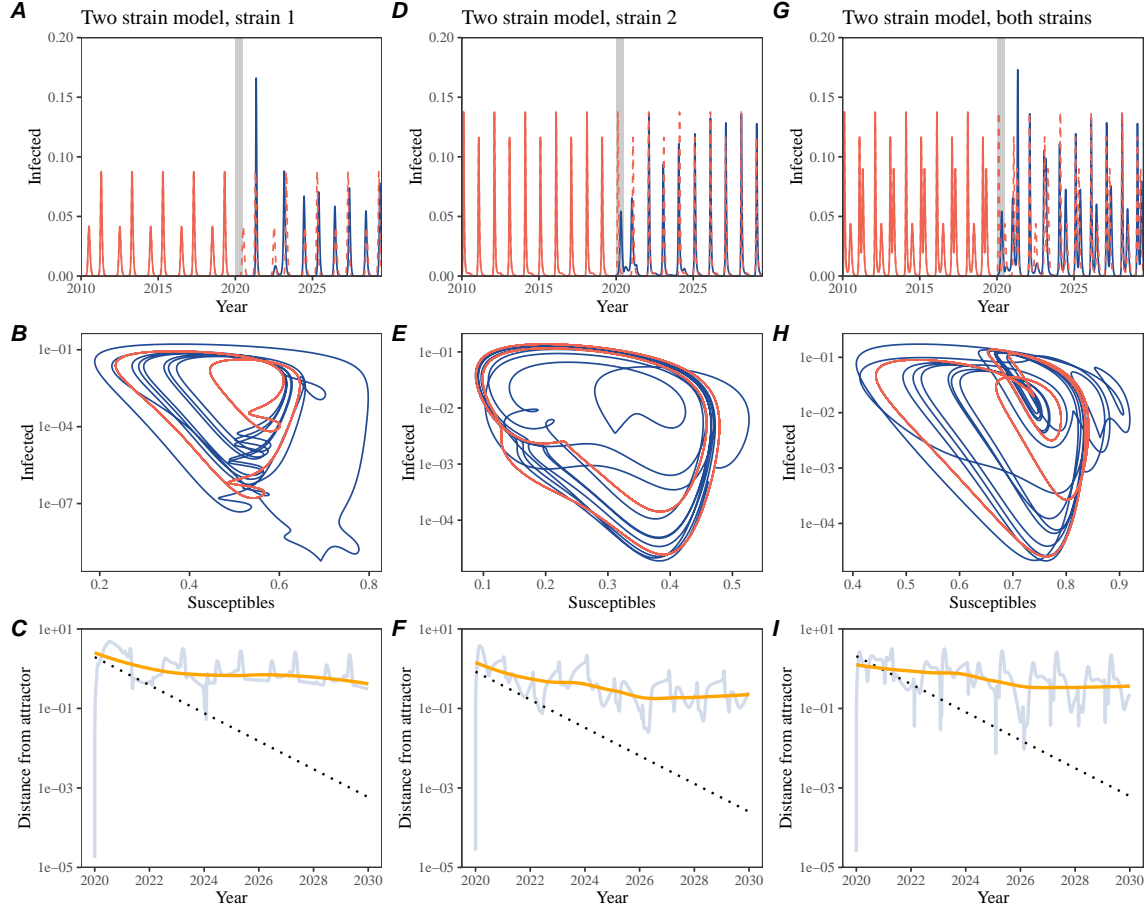


**Figure S4: A simple method to measure pathogen resilience following pandemic perturbations for a multi-strain system with strong seasonal forcing.** (A, D, G) Simulated epidemic trajectories using a multi-strain system with seasonal forcing (amplitude of 0.4). In this model, two strains compete through cross immunity. Red and blue solid lines represent epidemic dynamics before and after interventions are introduced, respectively. Red dashed lines represent counterfactual epidemic dynamics in the absence of interventions. Gray regions indicate the duration of interventions. (B, E, H) Phase plane representation of the time series in panels A, D, and G alongside the corresponding susceptible host dynamics. Red and blue solid lines represent epidemic trajectories on an SI phase plane before and after interventions are introduced, respectively. (C, F, I) Changes in logged distance from the attractor over time. Blue lines represent the logged distance from the attractor. Orange lines represent the locally estimated scatterplot smoothing (LOESS) fits to the logged distance from the attractor. Dotted lines show the intrinsic resilience of the seasonally unforced system.

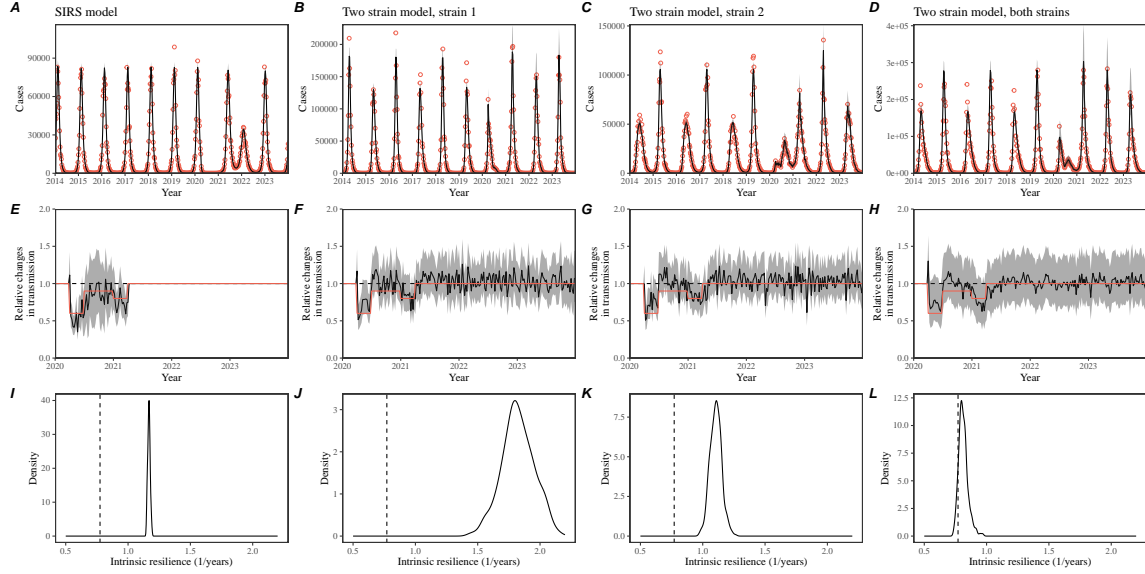


**Figure S5: Mechanistic model fits to simulated data and inferred intrinsic resilience.** We simulated discrete time, stochastic epidemic trajectories using seasonally forced SIRS model (A,E,I) and seasonally forced two-strain model (B–D, F–H, and J–L) and tested whether we can estimate the intrinsic resilience of the seasonally unforced versions of the model by fitting a mechanistic model (Supplementary Text). We fitted the same discrete time, deterministic SIRS model across all four scenarios. (A–D) Simulated case time series from corresponding models shown in the title (red) and SIRS model fits (black). (E–H) Assumed changes in transmission due to pandemic perturbations (red) and estimated time-varying relative transmission rates for the perturbation impact from the SIRS model fits (black). Solid lines and shaded regions represent fitted posterior median and 95% credible intervals. (I–L) True intrinsic resilience of the seasonally unforced system (vertical lines) and the posterior distribution of the inferred intrinsic resilience from the SIRS model (density plots).

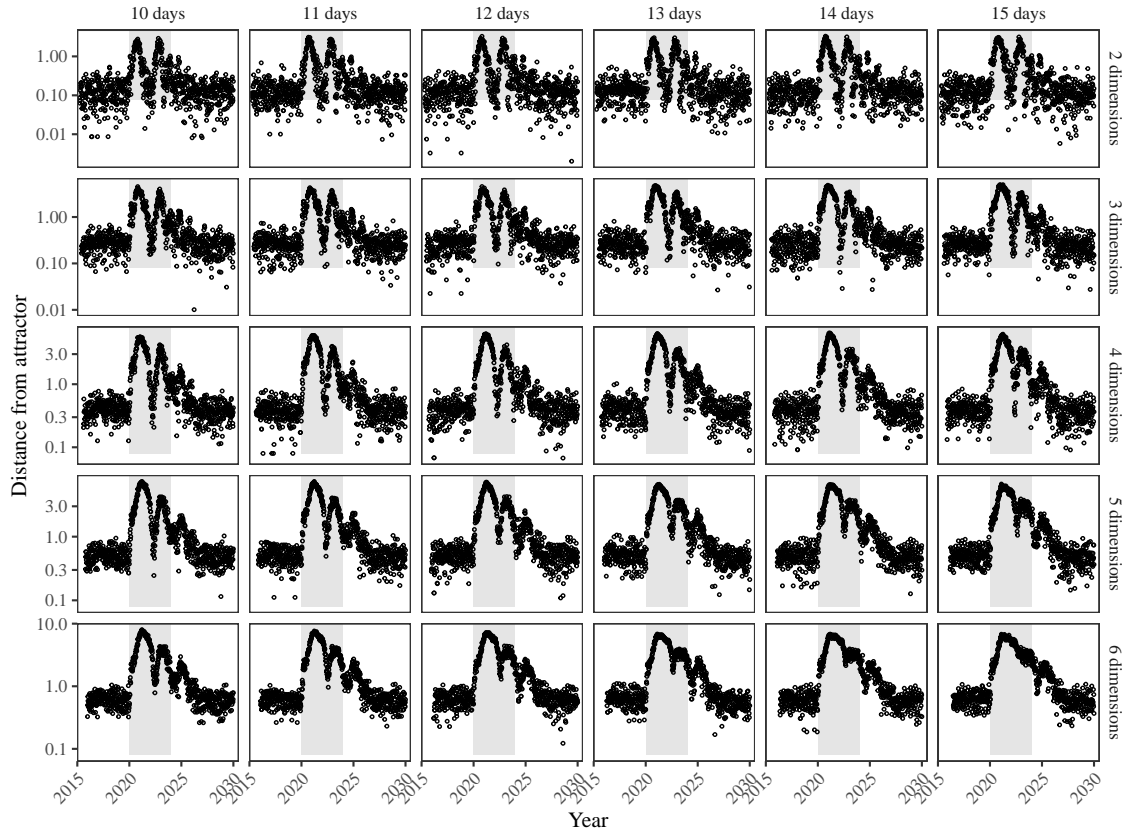


**Figure S6: Sensitivity of the distance from the attractor to choices about embedding lags and dimensions.** Sensitivity analysis for the distance-from-attractor time series shown in Figure 3E in the main text by varying the embedding lag between 10–15 days and embedding dimensions between 2–6 dimensions. [SWP: You said: “Did you do sensitivity analyses with other systems or just this one? I think we’ll probably need to do it with several systems”. I think it’s OK to just do this because we’re just trying to show qualitatively that longer lags and higher dimensions smooth things out. We also explore resilience of other models in other figures.]

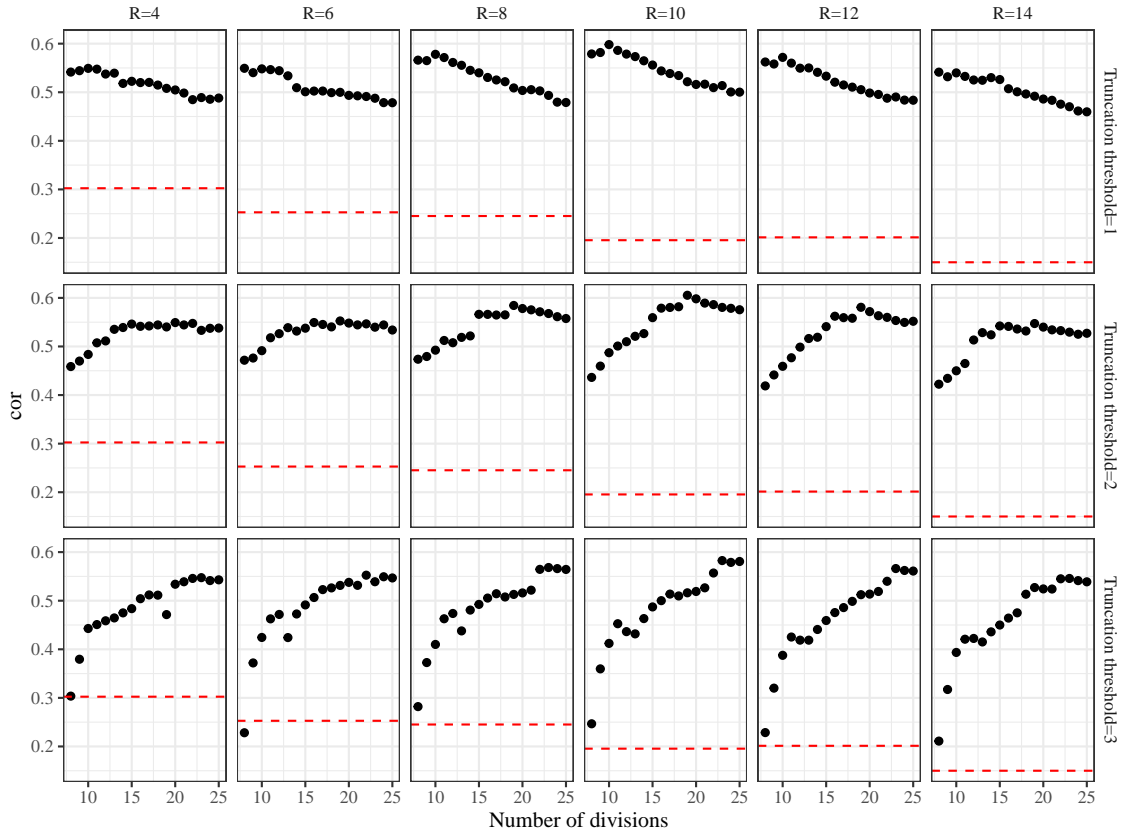


**Figure S7: Impact of fitting window selection on the estimation of empirical resilience.** We simulated 500 epidemics of a stochastic SIRS model with randomly drawn parameters and randomly generated pandemic perturbations (Supplementary Text). For each simulation, we varied the false nearest neighbor threshold  $R$  for reconstructing the empirical attractor as well as the parameters for regression window selection (i.e., the truncation threshold  $a$  and the the number of divisions  $K$ ). Each point represents the resulting correlation coefficient between empirical and intrinsic resilience estimates for a given scenario. Dashed lines represent the correlation coefficient between empirical and intrinsic resilience estimates for the naive approach that fits a linear regression on a log scale, starting from the maximum distance until the end of the time series.

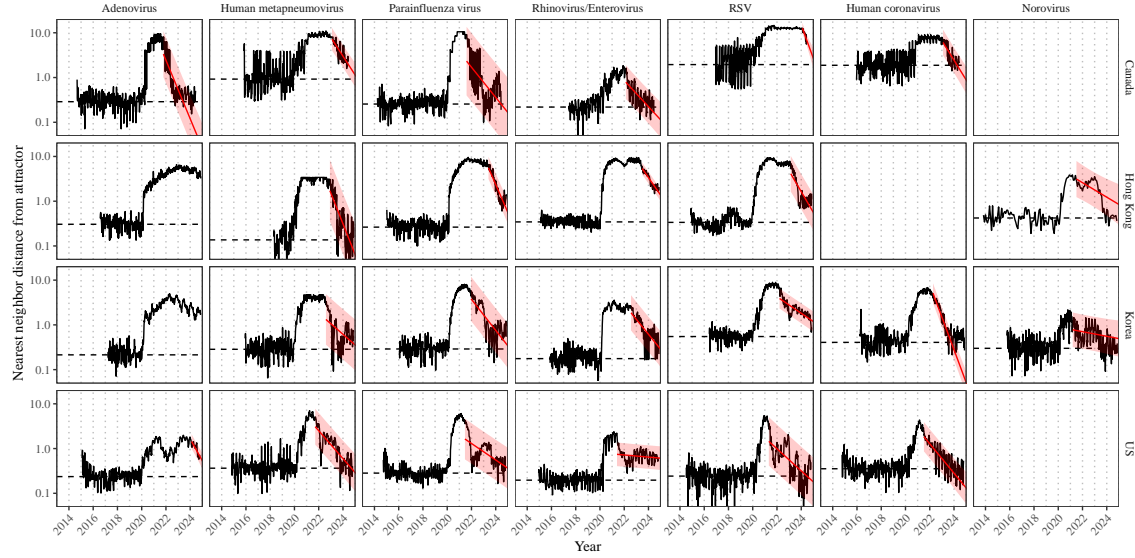


**Figure S8: Estimated time series of distance from the attractor for each pathogen and corresponding linear regression fits using automated window selection criterion across Canada, Hong Kong, Korea, and the US.** Black lines represent the estimated distance from the attractor. Red lines and shaded regions represent the linear regression fits and corresponding 95% confidence intervals. Dashed lines represent the average of the pre-pandemic nearest neighbor distances.

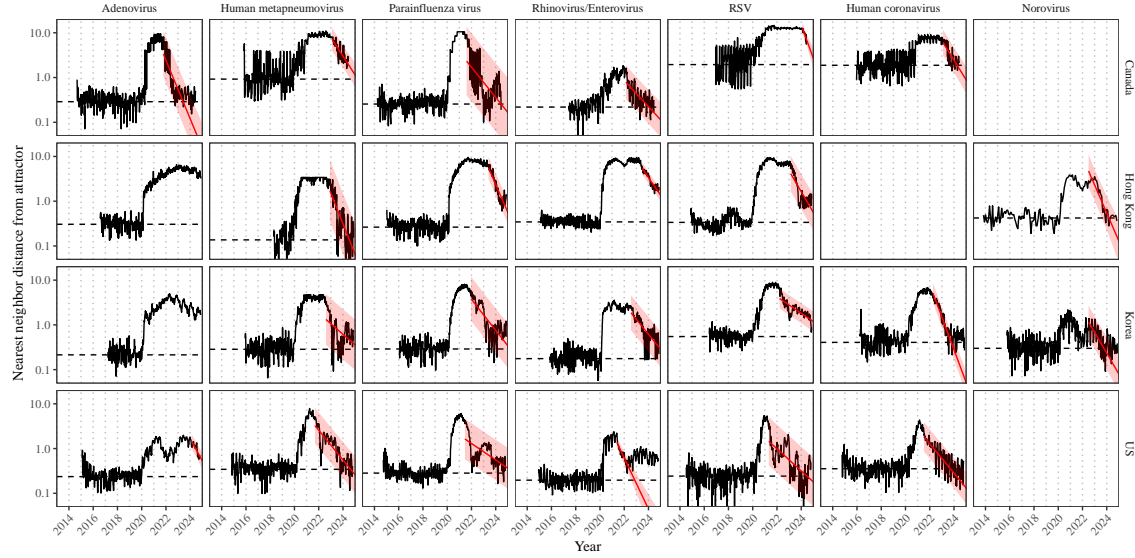


**Figure S9: Estimated time series of distance from the attractor for each pathogen and corresponding linear regression fits across Canada, Hong Kong, Korea, and the US, including ad-hoc regression window selection.** We used ad-hoc regression windows for norovirus in Hong Kong and Korea and Rhinovirus/Enterovirus in the US. Black lines represent the estimated distance from the attractor. Red lines and shaded regions represent the linear regression fits and corresponding 95% confidence intervals. Dashed lines represent the average of the pre-pandemic nearest neighbor distances.

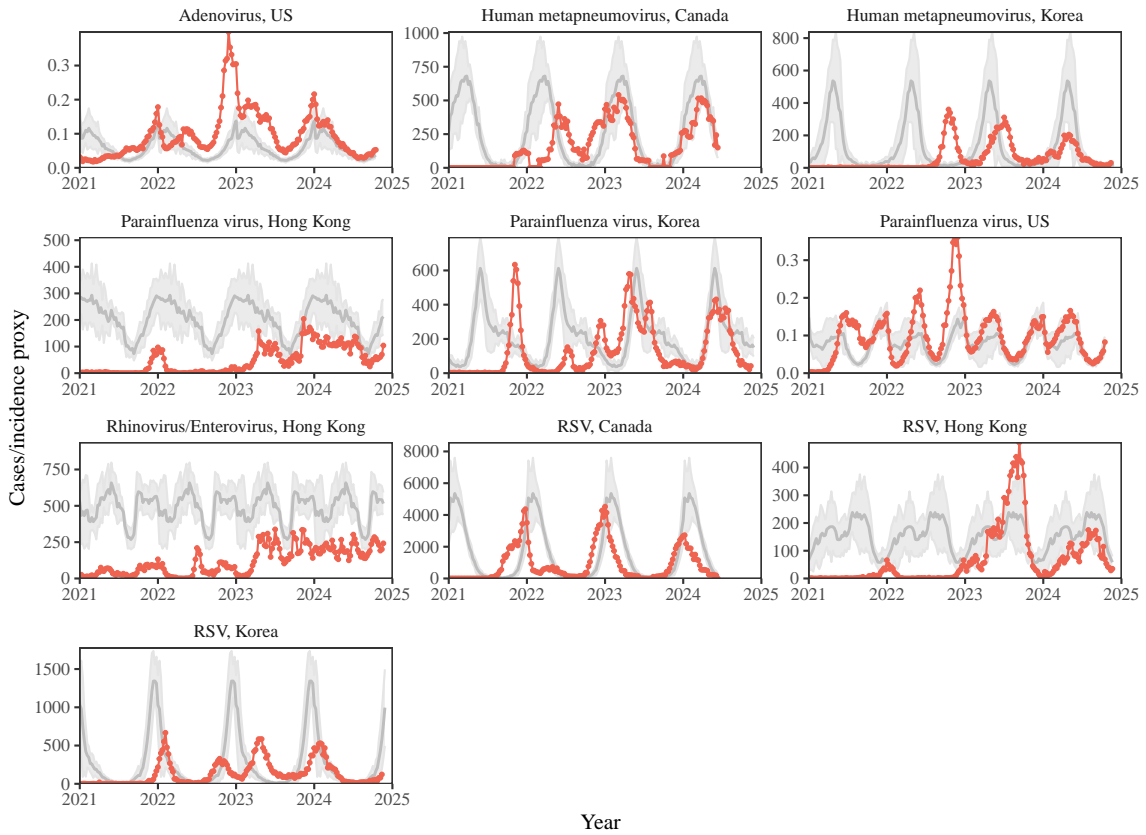


**Figure S10: Observed dynamics for pathogen that are predicted to return after the end of 2024.** Red points and lines represent data before 2020. Gray lines and shaded regions represent the mean seasonal patterns and corresponding 95% confidence intervals around the mean, previously shown in Figure 1.

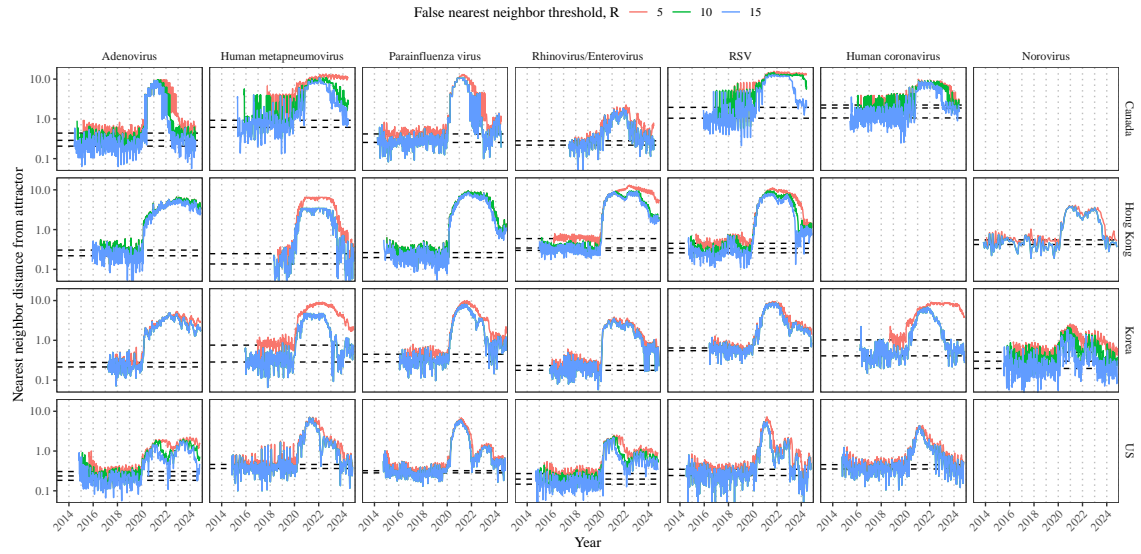


**Figure S11: Estimated time series of distance from the attractor for each pathogen across different choices about false nearest neighbor threshold values.** Using higher threshold values for the false nearest neighbor approach gives lower embedding dimensions. Colored lines represent the estimated distance from the attractor for different threshold values.

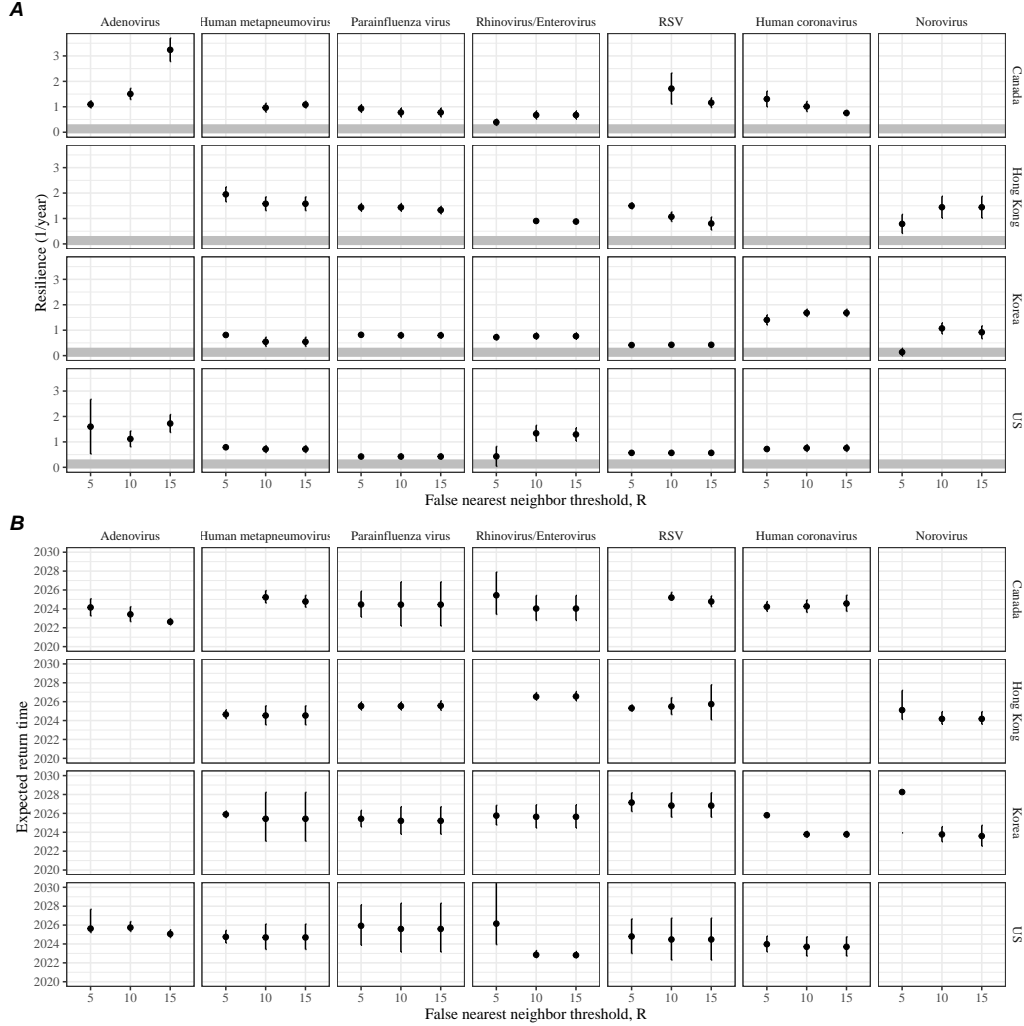


**Figure S12: Summary of resilience estimates and predictions for return time across different choices about false nearest neighbor threshold values.** The automated window selection method was used for all scenarios to estimate pathogen resilience, except for norovirus in Hong Kong and Korea and Rhinovirus/Enterovirus in the US. We used the same ad-hoc regression windows for norovirus in Hong Kong and Korea and Rhinovirus/Enterovirus in the US as we did in the main analysis. (A) Estimated pathogen resilience. The gray horizontal line represents the intrinsic resilience of pre-vaccination measles dynamics. (B) Predicted timing of when each pathogen will return to their pre-pandemic cycles. The dashed line in panel B indicates the end of 2024. Error bars represent 95% confidence intervals.

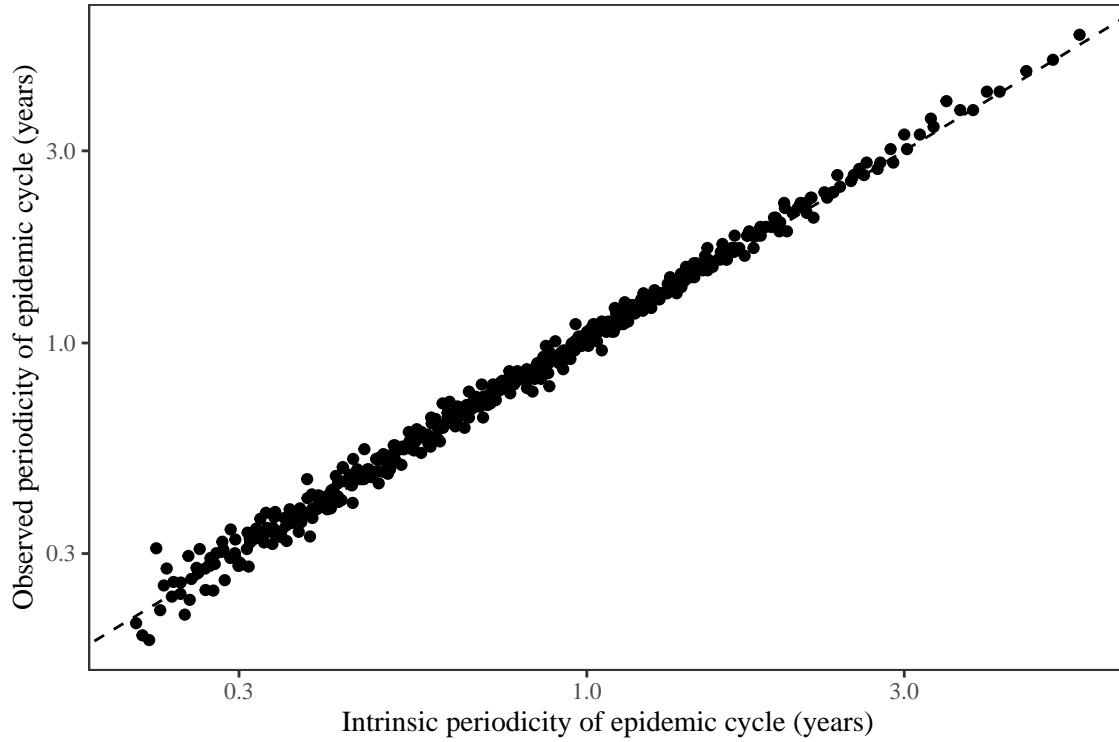


Figure S13: **Comparison between the observed and intrinsic periodicity of the epidemic cycle of the seasonally unforced SIRS model.** The observed periodicity of the epidemic corresponds to the periodicity at which maximum spectral density occurs. The intrinsic periodicity of the epidemic corresponds to  $2\pi/\text{Im}(\lambda)$ , where  $\text{Im}(\lambda)$  is the imaginary part of the eigenvalue.

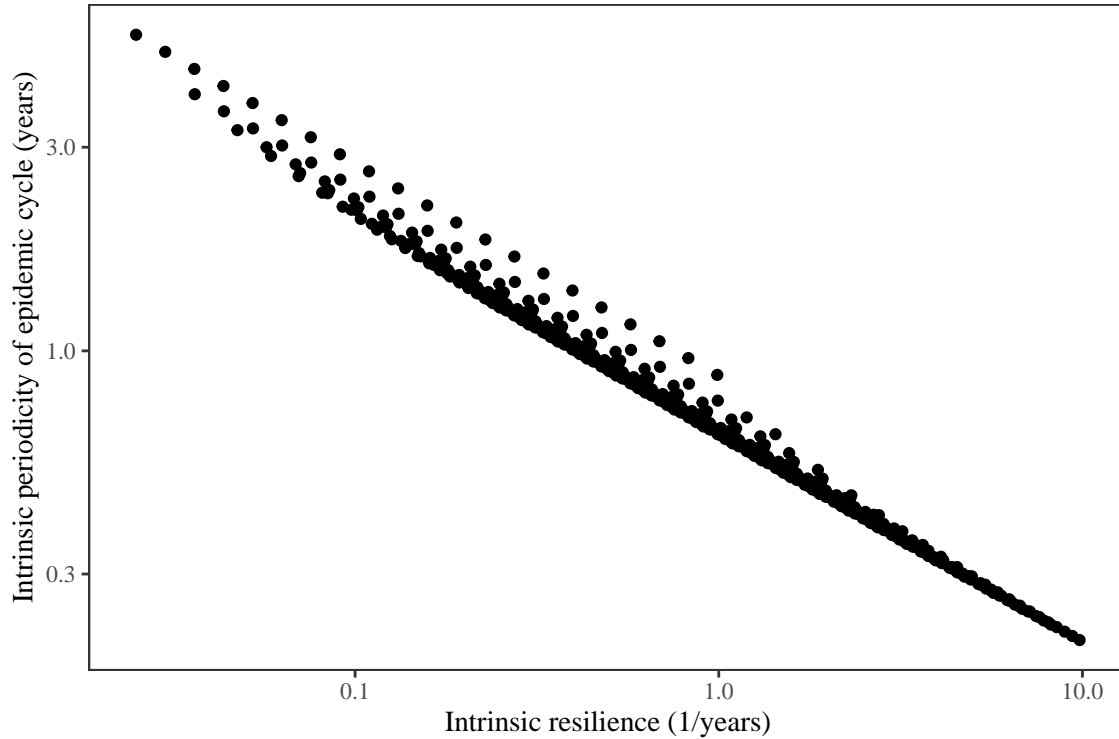


Figure S14: **Comparison between the intrinsic resilience and periodicity of the epidemic cycle of the seasonally unforced SIRS model.** The intrinsic resilience of the epidemic corresponds to the negative of the real value of the eigenvalue  $-\text{Re}(\lambda)$ . The intrinsic periodicity of the epidemic corresponds to  $2\pi/\text{Im}(\lambda)$ , where  $\text{Im}(\lambda)$  is the imaginary part of the eigenvalue.

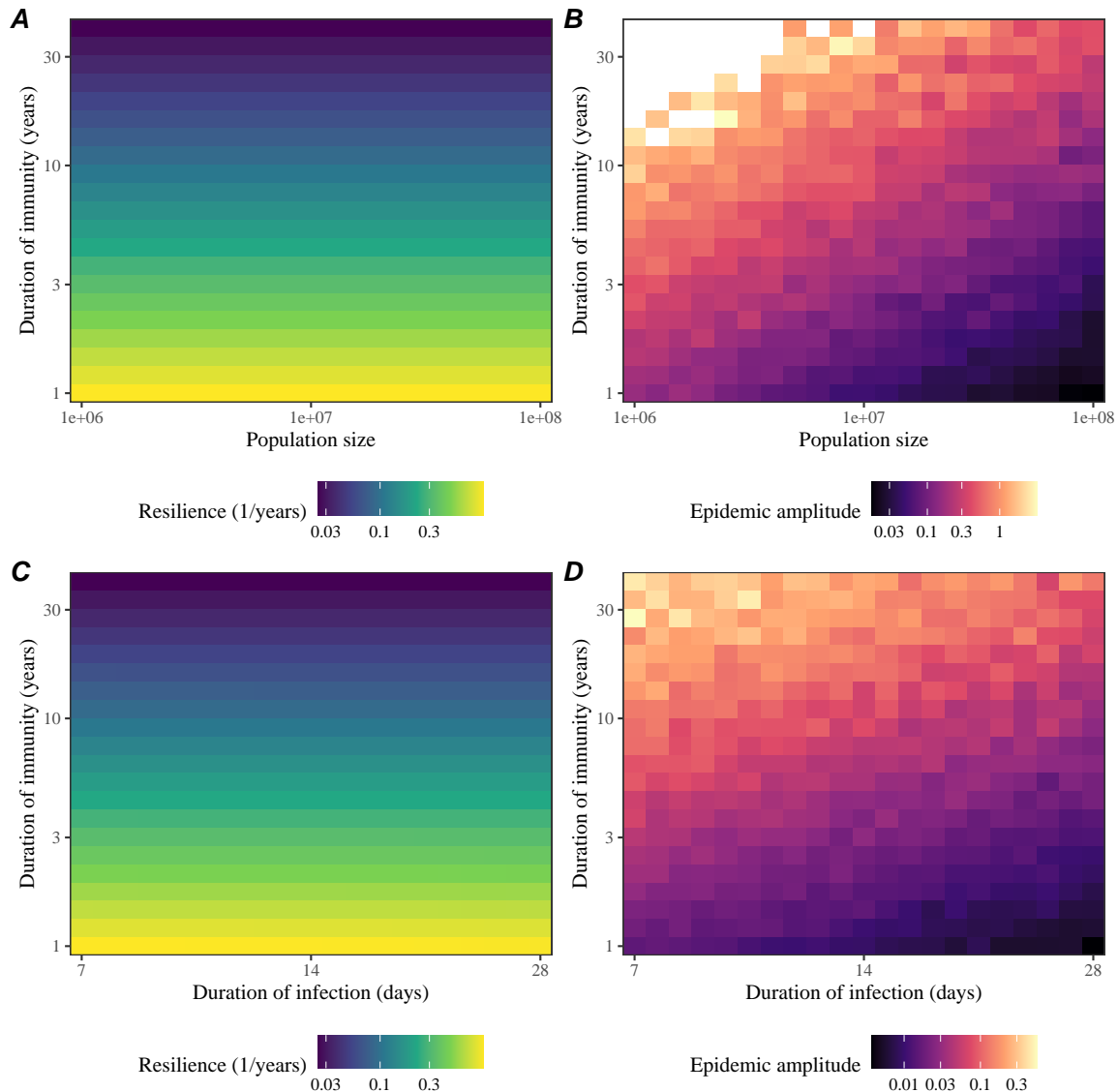
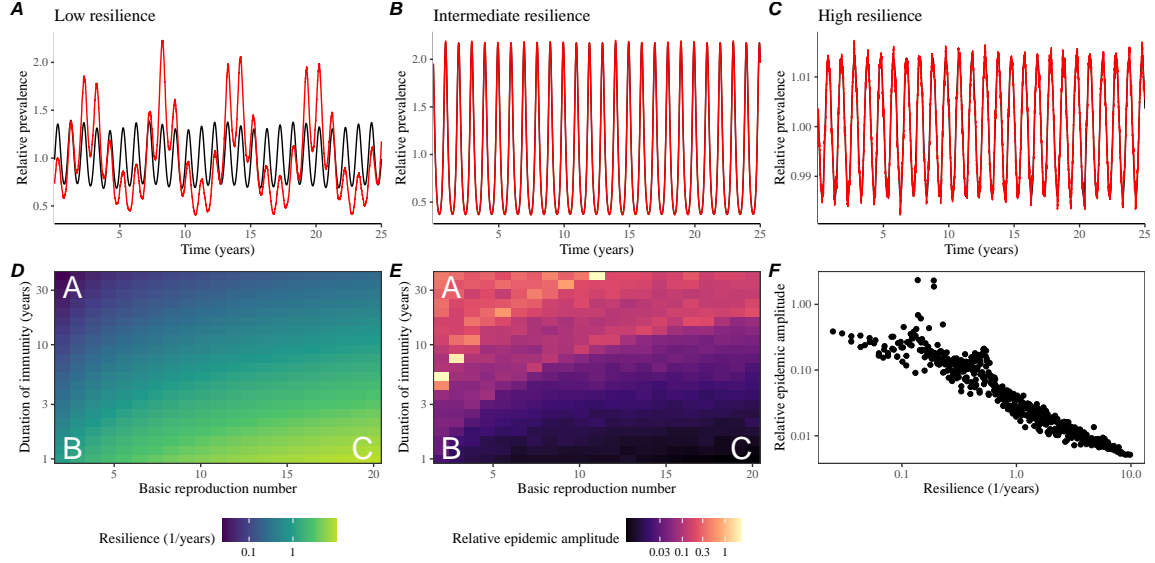


Figure S15: **Impact of population size and the average duration of infection of a host-pathogen system to its sensitivity to stochastic perturbations.** (A) Intrinsic resilience of a system as a function of population size and the average duration of immunity. (B) Epidemic amplitude as a function of population size and the average duration of immunity. (C) Intrinsic resilience of a system as a function of the average duration of infection and the average duration of immunity. (D) Epidemic amplitude as a function of the average duration of infection and the average duration of immunity. The epidemic amplitude corresponds to  $(\max I - \min I)/(2\bar{I})$ , where  $\bar{I}$  represents the mean prevalence.



**Figure S16: Linking resilience of a host-pathogen system to its sensitivity to stochastic perturbations for the seasonally forced SIRS model.** (A–C) Epidemic trajectories of a stochastic SIRS model across three different resilience values: low, intermediate, and high. The relative prevalence was calculated by dividing infection prevalence by its mean value. (D) The heat map represents the intrinsic resilience of the seasonally unforced system as a function of the basic reproduction number  $\mathcal{R}_0$  and the duration of immunity. (E) The heat map represents the relative epidemic amplitude as a function of the basic reproduction number  $\mathcal{R}_0$  and the duration of immunity. To calculate the relative epidemic amplitude, we first take the relative difference in infection prevalence between stochastic and deterministic trajectories:  $\epsilon = (I_{\text{stoch}} - I_{\text{det}})/I_{\text{det}}$ . Then, we calculate the difference between maximum and minimum of the relative difference and divide by half:  $(\max \epsilon - \min \epsilon)/2$ . (F) The relationship between pathogen resilience and relative epidemic amplitude.

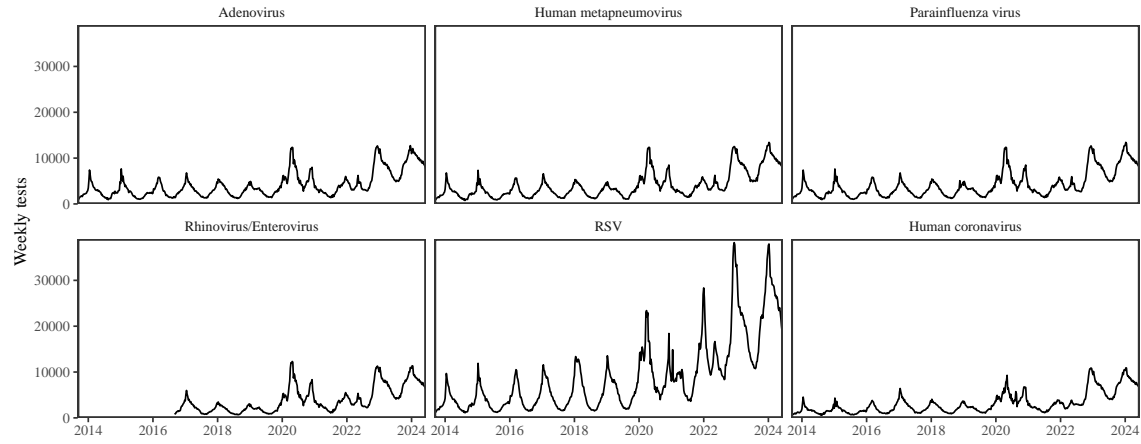


Figure S17: Testing patterns for respiratory pathogens in Canada.

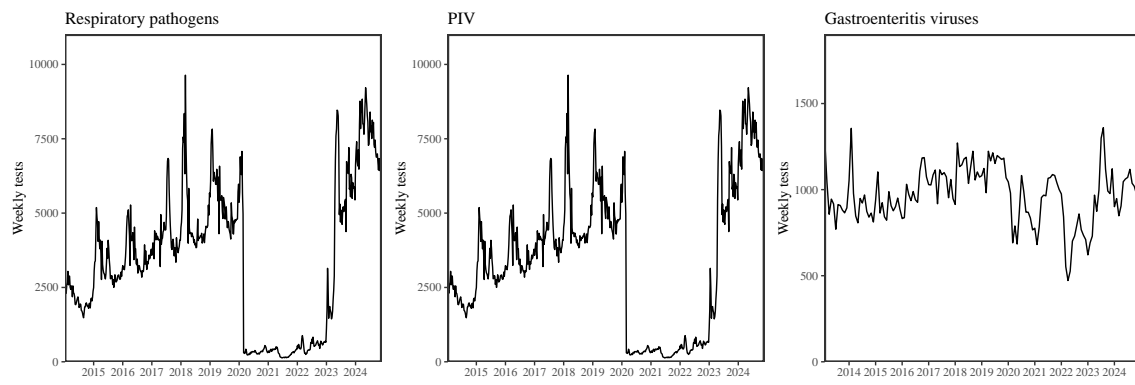


Figure S18: Testing patterns for respiratory pathogens, PIV, and gastroenteritis viruses in Hong Kong.

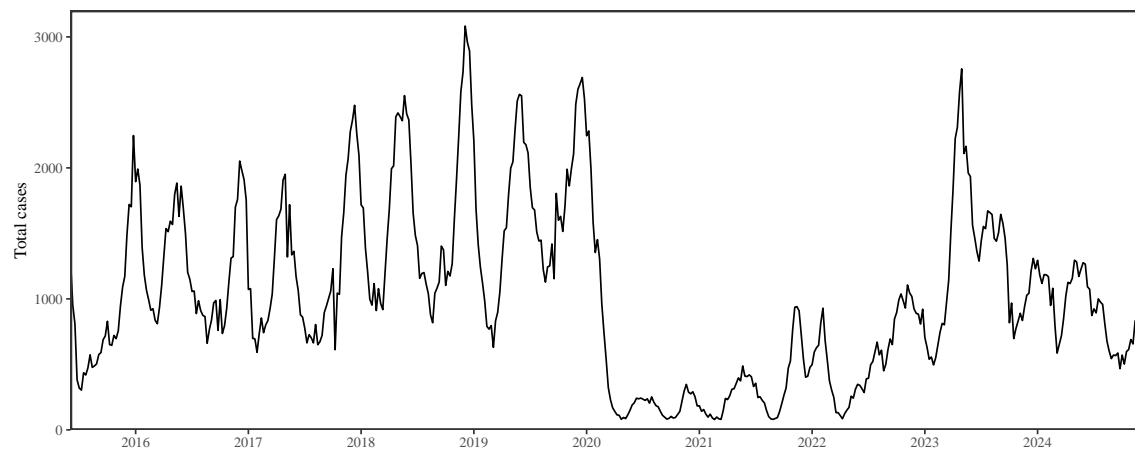


Figure S19: Total number of reported respiratory infection cases in Korea.

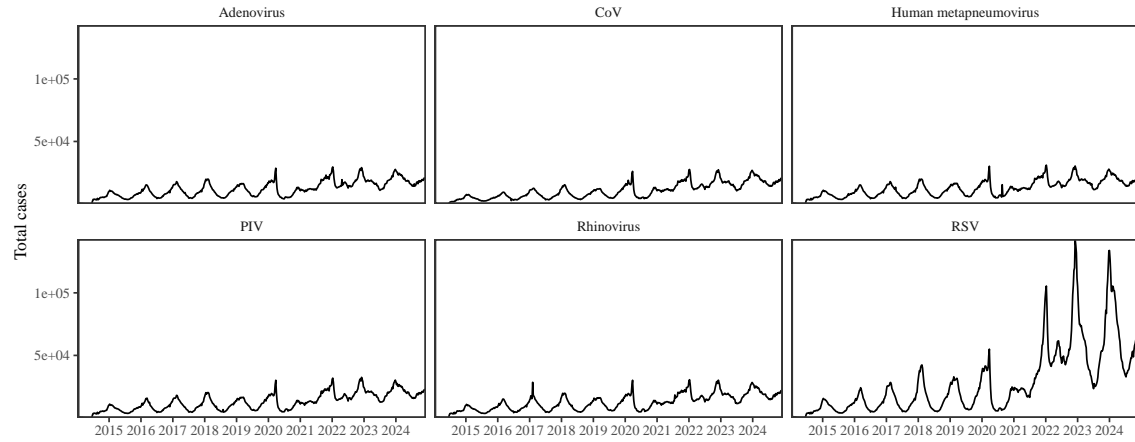


Figure S20: Testing patterns for respiratory pathogens in the US reported through the NREVSS.

## 744 References

- 745 [1] Rachel E Baker, Sang Woo Park, Wenchang Yang, Gabriel A Vecchi, C Jessica E  
746 Metcalf, and Bryan T Grenfell. The impact of COVID-19 nonpharmaceutical  
747 interventions on the future dynamics of endemic infections. *Proceedings of the*  
748 *National Academy of Sciences*, 117(48):30547–30553, 2020.
- 749 [2] Gabriela B Gomez, Cedric Mahé, and Sandra S Chaves. Uncertain effects of the  
750 pandemic on respiratory viruses. *Science*, 372(6546):1043–1044, 2021.
- 751 [3] Mihaly Koltai, Fabienne Krauer, David Hodgson, Edwin van Leeuwen, Marina  
752 Treskova-Schwarzbach, Mark Jit, and Stefan Flasche. Determinants of RSV  
753 epidemiology following suppression through pandemic contact restrictions. *Epi-*  
754 *demics*, 40:100614, 2022.
- 755 [4] Sang Woo Park, Brooklyn Noble, Emily Howerton, Bjarke F Nielsen, Sarah  
756 Lentz, Lilliam Ambroggio, Samuel Dominguez, Kevin Messacar, and Bryan T  
757 Grenfell. Predicting the impact of non-pharmaceutical interventions against  
758 COVID-19 on *Mycoplasma pneumoniae* in the United States. *Epidemics*,  
759 49:100808, 2024.
- 760 [5] Amanda C Perofsky, Chelsea L Hansen, Roy Burstein, Shanda Boyle, Robin  
761 Prentice, Cooper Marshall, David Reinhart, Ben Capodanno, Melissa Truong,  
762 Kristen Schwabe-Fry, et al. Impacts of human mobility on the citywide trans-  
763 mission dynamics of 18 respiratory viruses in pre-and post-COVID-19 pandemic  
764 years. *Nature communications*, 15(1):4164, 2024.
- 765 [6] Eric J Chow, Timothy M Uyeki, and Helen Y Chu. The effects of the COVID-19  
766 pandemic on community respiratory virus activity. *Nature Reviews Microbiol-*  
767 *ogy*, 21(3):195–210, 2023.
- 768 [7] Stephen M Kissler, Christine Tedijanto, Edward Goldstein, Yonatan H Grad,  
769 and Marc Lipsitch. Projecting the transmission dynamics of SARS-CoV-2  
770 through the postpandemic period. *Science*, 368(6493):860–868, 2020.
- 771 [8] Rachel E Baker, Chadi M Saad-Roy, Sang Woo Park, Jeremy Farrar, C Jessica E  
772 Metcalf, and Bryan T Grenfell. Long-term benefits of nonpharmaceutical inter-  
773 ventions for endemic infections are shaped by respiratory pathogen dynamics.  
774 *Proceedings of the National Academy of Sciences*, 119(49):e2208895119, 2022.
- 775 [9] Maaike C Swets, Clark D Russell, Ewen M Harrison, Annemarie B Docherty,  
776 Nazir Lone, Michelle Girvan, Hayley E Hardwick, Leonardus G Visser, Pe-  
777 ter JM Openshaw, Geert H Groeneveld, et al. SARS-CoV-2 co-infection with  
778 influenza viruses, respiratory syncytial virus, or adenoviruses. *The Lancet*,  
779 399(10334):1463–1464, 2022.

- 780 [10] Chun-Yang Lin, Joshua Wolf, David C Brice, Yilun Sun, Macauley Locke,  
781 Sean Cherry, Ashley H Castellaw, Marie Wehenkel, Jeremy Chase Crawford,  
782 Veronika I Zarnitsyna, et al. Pre-existing humoral immunity to human common  
783 cold coronaviruses negatively impacts the protective SARS-CoV-2 antibody re-  
784 sponse. *Cell host & microbe*, 30(1):83–96, 2022.
- 785 [11] Sam M Murray, Azim M Ansari, John Frater, Paul Klenerman, Susanna  
786 Dunachie, Eleanor Barnes, and Ane Ogbe. The impact of pre-existing cross-  
787 reactive immunity on SARS-CoV-2 infection and vaccine responses. *Nature*  
788 *Reviews Immunology*, 23(5):304–316, 2023.
- 789 [12] John-Sebastian Eden, Chisha Sikazwe, Ruopeng Xie, Yi-Mo Deng, Sheena G  
790 Sullivan, Alice Michie, Avram Levy, Elena Cutmore, Christopher C Blyth,  
791 Philip N Britton, et al. Off-season RSV epidemics in Australia after easing  
792 of COVID-19 restrictions. *Nature communications*, 13(1):2884, 2022.
- 793 [13] Stuart L Pimm. The structure of food webs. *Theoretical population biology*,  
794 16(2):144–158, 1979.
- 795 [14] Michael G Neubert and Hal Caswell. Alternatives to resilience for measuring  
796 the responses of ecological systems to perturbations. *Ecology*, 78(3):653–665,  
797 1997.
- 798 [15] Lance H Gunderson. Ecological resilience—in theory and application. *Annual*  
799 *review of ecology and systematics*, 31(1):425–439, 2000.
- 800 [16] Vasilis Dakos and Sonia Kéfi. Ecological resilience: what to measure and how.  
801 *Environmental Research Letters*, 17(4):043003, 2022.
- 802 [17] Floris Takens. Detecting strange attractors in turbulence. In *Dynamical Sys-*  
803 *tems and Turbulence, Warwick 1980: proceedings of a symposium held at the*  
804 *University of Warwick 1979/80*, pages 366–381. Springer, 2006.
- 805 [18] Jonathan Dushoff, Joshua B Plotkin, Simon A Levin, and David JD Earn.  
806 Dynamical resonance can account for seasonality of influenza epidemics. *Pro-*  
807 , 101(48):16915–16916, 2004.
- 808 [19] Alan Hastings, Karen C Abbott, Kim Cuddington, Tessa Francis, Gabriel Gell-  
809 ner, Ying-Cheng Lai, Andrew Morozov, Sergei Petrovskii, Katherine Scran-  
810 ton, and Mary Lou Zeeman. Transient phenomena in ecology. *Science*,  
811 361(6406):eaat6412, 2018.
- 812 [20] Matthew B Kennel, Reggie Brown, and Henry DI Abarbanel. Determining  
813 embedding dimension for phase-space reconstruction using a geometrical con-  
814 struction. *Physical review A*, 45(6):3403, 1992.

- 815 [21] Eugene Tan, Shannon Algar, Débora Corrêa, Michael Small, Thomas Stemler,  
816 and David Walker. Selecting embedding delays: An overview of embedding  
817 techniques and a new method using persistent homology. *Chaos: An Interdis-*  
818 *ciplinary Journal of Nonlinear Science*, 33(3), 2023.
- 819 [22] Jennifer M Radin, Anthony W Hawksworth, Peter E Kammerer, Melinda Bal-  
820 ansay, Rema Raman, Suzanne P Lindsay, and Gary T Brice. Epidemiology  
821 of pathogen-specific respiratory infections among three US populations. *PLoS*  
822 *One*, 9(12):e114871, 2014.
- 823 [23] Guojian Lv, Limei Shi, Yi Liu, Xuecheng Sun, and Kai Mu. Epidemiological  
824 characteristics of common respiratory pathogens in children. *Scientific Reports*,  
825 14(1):16299, 2024.
- 826 [24] Saverio Caini, Adam Meijer, Marta C Nunes, Laetitia Henaff, Malaika Zounon,  
827 Bronke Boudewijns, Marco Del Riccio, and John Paget. Probable extinction of  
828 influenza b/yamagata and its public health implications: a systematic literature  
829 review and assessment of global surveillance databases. *The Lancet Microbe*,  
830 2024.
- 831 [25] Zhiyuan Chen, Joseph L-H Tsui, Bernardo Gutierrez, Simon Busch Moreno,  
832 Louis du Plessis, Xiaowei Deng, Jun Cai, Sumali Bajaj, Marc A Suchard,  
833 Oliver G Pybus, et al. COVID-19 pandemic interventions reshaped the global  
834 dispersal of seasonal influenza viruses. *Science*, 386(6722):eadq3003, 2024.
- 835 [26] Bryan T Grenfell, Ottar N Bjørnstad, and Bärbel F Finkenstädt. Dynamics of  
836 measles epidemics: scaling noise, determinism, and predictability with the TSIR  
837 model. *Ecological monographs*, 72(2):185–202, 2002.
- 838 [27] Samit Bhattacharyya, Per H Gesteland, Kent Korgenski, Ottar N Bjørnstad,  
839 and Frederick R Adler. Cross-immunity between strains explains the dynamical  
840 pattern of paramyxoviruses. *Proceedings of the National Academy of Sciences*,  
841 112(43):13396–13400, 2015.
- 842 [28] Virginia E Pitzer, Cécile Viboud, Vladimir J Alonso, Tanya Wilcox, C Jessica  
843 Metcalf, Claudia A Steiner, Amber K Haynes, and Bryan T Grenfell. Environ-  
844 mental drivers of the spatiotemporal dynamics of respiratory syncytial virus in  
845 the United States. *PLoS pathogens*, 11(1):e1004591, 2015.
- 846 [29] Katharine R Dean, Fabienne Krauer, Lars Walløe, Ole Christian Lingjærde, Bar-  
847 bara Bramanti, Nils Chr Stenseth, and Boris V Schmid. Human ectoparasites  
848 and the spread of plague in Europe during the Second Pandemic. *Proceedings*  
849 *of the National Academy of Sciences*, 115(6):1304–1309, 2018.
- 850 [30] Margarita Pons-Salort and Nicholas C Grassly. Serotype-specific immunity  
851 explains the incidence of diseases caused by human enteroviruses. *Science*,  
852 361(6404):800–803, 2018.

- 853 [31] Sarah Cobey and Edward B Baskerville. Limits to causal inference with state-  
854 space reconstruction for infectious disease. *PLoS one*, 11(12):e0169050, 2016.
- 855 [32] Public Health Agency of Canada. Respiratory virus detections in  
856 Canada. 2024. <https://www.canada.ca/en/public-health/services/surveillance/respiratory-virus-detections-canada.html>. Accessed Sep  
857 4, 2024.
- 858 [33] Centre for Health Protection. Detection of pathogens from respiratory spec-  
859 imens. 2024. <https://www.chp.gov.hk/en/statistics/data/10/641/642/2274.html>. Accessed Nov 20, 2024.
- 860 [34] Centre for Health Protection. Detection of gastroenteritis viruses from faecal  
861 specimens. 2024. <https://www.chp.gov.hk/en/statistics/data/10/641/717/3957.html>. Accessed Nov 20, 2024.
- 862 [35] Korea Disease Control and Prevention Agency. Acute respiratory infection,  
863 Sentinel surveillance infectious diseases. 2024. <https://dportal.kdca.go.kr/pot/is/st/ari.do>. Accessed Nov 20, 2024.
- 864 [36] Edward Goldstein, Sarah Cobey, Saki Takahashi, Joel C Miller, and Marc Lipsitch.  
Predicting the epidemic sizes of influenza A/H1N1, A/H3N2, and B: a statistical method. *PLoS medicine*, 8(7):e1001051, 2011.
- 865 [37] Bob Carpenter, Andrew Gelman, Matthew D Hoffman, Daniel Lee, Ben  
866 Goodrich, Michael Betancourt, Marcus A Brubaker, Jiqiang Guo, Peter Li,  
867 and Allen Riddell. Stan: A probabilistic programming language. *Journal of  
868 statistical software*, 76, 2017.
- 869 [38] Stan Development Team. RStan: the R interface to Stan, 2024. R package  
870 version 2.32.6.